Journal of Inorganic and General Chemistry
ZAAC
Zeitschrift für anorganische und allgemeine Chemie
www.zaac.wiley-vch.de
RESEARCH ARTICLE

DOI: 10.1002/zaac.202500198

Fine-Tuned Magnetic and Electrochemical Properties of a Series of Fe(II) Complexes with Asymmetric Jäger-Type $(N_2O_2)^{2-}$ Ligands

Constantin Schreck, Frank. W. Heinemann, Phil Köhler, Gerald Hörner,* and Birgit Weber*

Dedicated to Prof. Franc Meyer and Prof. Christian Limberg on the occasion of their 60th birthdays

A series of seven new asymmetrically substituted Jäger-type $(N_2O_2)^{2-}$ ligands and their iron(II) complexes is reported, designed to probe how mixed substitution influences molecular and material properties. Comprehensive characterization—including magnetic measurements, X-ray diffraction, spectroscopy, electrochemistry, and density functional theory (DFT) calculations—shows that many optical and redox properties of the asymmetric ligands and complexes follow additive trends from their symmetric counterparts. Cyclic voltammetry reveals predictable fine-tuning of the $Fe^{3+/2+}$ redox potential, while DFT calculations confirm the decisive role of carbonyl coordination: ketone donors enable spin-crossover (SCO), whereas ester donors stabilize the high-spin state. However, the SCO behavior of the bulk iron(II) materials often deviates; in some cases, SCO is suppressed, while in others, entirely new transition profiles appear. These findings highlight the decisive role of molecular symmetry and intermolecular packing in governing cooperativity in SCO materials.

1. Introduction

The Jäger-ligand family and metal complexes thereof have been extensively studied in various contexts, spanning bioinorganic chemistry, spin-state switching, and electrocatalysis.[1,2] The ready synthetic access and broad tunability of the tetradentate, dianionic keto-enamine ligands render these scaffolds chemically and sterically adaptable to the selected chemical problem. Recently, these ligand scaffolds have supported coordination-activated emission in closed-shell complexes,[3,4] and coordination-induced emission quenching in open-shell complexes,[5] respectively. The most prominent utility of Jäger ligands is arguably the spin switching in 3d-metal complexes, which feature N_2O_2 coordination sites with phenylenediamine backbones.[6–10] These systems are of interest due to their potential for temperature-induced spin-crossover (SCO)[11–19] behavior in iron(II) complexes, as well as coordination-induced spin-state switching[20–24] observed in corresponding nickel(II) complexes.

To introduce additional functionalities—such as amphiphilicity,[25,26] redox activity,[27,28] and fluorescence[5]—the ligands can be functionalized via substitution on the phenylene backbone. These modifications are typically introduced at early synthetic stages on the "preligand", prior to the formation of the more sensitive Schiff-base-like ligands.

An alternative strategy for the coarse tuning of ligand and complex properties involves the modification/exchange of substituents directly adjacent to the chelate ring. In the case of Salen and Salophen-type ligands, this is realized through differently substituted salicylic aldehydes, leading to a wide range of different functionalities.[29–35] For the Jäger-type ligands, this is achieved by selecting suitable keto-enol ethers (KEE) for condensation with the diamine, thus yielding Jäger-ligands bearing diverse enamine substituents. These functional groups can significantly influence redox behavior, stability, solubility, coordination strength, and spin state. While some "passive" substituents induce only subtle changes, others drastically alter the electronic structure, (de)stabilize specific metal oxidation states, or modulate SCO activity in both solid state and in solution.[36–38]

Most Jäger-type complexes reported to date feature (idealized) C_{2v}-symmetric ligands, where both enamine moieties feature identical substituents. Asymmetry within these ligands is generally restricted to the phenylene backbone[10] and arises due to steric or synthetic constraints, rather than as a deliberate design feature. Such backbone asymmetry tends to exert diffuse, nondirectional effects on the metal center. In previous studies of iron(II) complexes with such symmetric phenylene diamine-derived Jäger ligands,[10] we observed that SCO behavior is highly dependent on ligand substitution. Certain substituents were

C. Schreck, P. Köhler, G. Hörner, B. Weber
Institute for Inorganic and Analytical Chemistry, Friedrich-Schiller-University Jena, Humboldtstraße 8, 07743 Jena, Germany
E-mail: gerald.hoerner@uni-jena.de; birgit.weber@uni-jena.de
C. Schreck
Department of Chemistry, Inorganic Chemistry II, University of Bayreuth, Universitätsstraße 30, 95447 Bayreuth, Germany
F. W. Heinemann
Department of Chemistry and Pharmacy, Inorganic Chemistry, Friedrich-Alexander-University Erlangen-Nürnberg (FAU), Egerlandstraße 3, 91058 Erlangen, Germany

Supporting information for this article is available on the WWW under https://doi.org/10.1002/zaac.202500198

found to completely inhibit SCO, both in the solid state and in solution. Density functional theory (DFT) calculations of the relative SCO energies across the substitution series supported these findings, highlighting the nature of the coordinating oxygen atom as a key determinant in enabling or impeding SCO.

Fine-tuning of the ligands and complexes' properties, therefore, suggests structure interpolation between two different symmetric scaffolds. In the case of tetradentate Schiff-base ligands, introducing different substituents on each side of the chelate ring offers a more targeted approach for the fine-tuning of properties. The mixed-substitution pattern has been scarcely used so far. However, the boost of structure variation holds promise of novel properties—such as enhanced solubility and altered crystal packing—that are inaccessible to their symmetric counterparts. Mixed substitution has previously been explored in related Salen-type ligands,[39] but has rarely been applied to Jäger systems.[40–48] In a recent study, Villamann et al.[49] reported asymmetric ligands simultaneously consisting of one salophen- and one Jäger-type chelate arm. The authors reported on the anticancer activity of the respective nickel(II) and zinc(II) complexes. With respect to SCO, we are aware of only a single preceding study on asymmetric Jäger ligands. Therein, our group reported on asymmetric Jäger ligands with mixed substituents,[50] yielding the iron(II) complexes $[FeL^{12}(py)_2]$, $[FeL^{13}(py)_2]$, and $[FeL^{23}(py)_2]$, which were compared to their C_{2v}-symmetric analogs (for ligand notation, see **Scheme 1**, left). $[FeL^{13}(py)_2]$ with a mixed ketone/ester coordination sphere showcases the fine-tuning abilities enabled by asymmetric substitution. This complex underwent SCO in the solid, whereas the parent complex $[FeL^{33}(py)_2]$ with an ester/ester coordination was inactive, remaining in the preferred high-spin (HS) state.

In this work, we expand the library of asymmetric Jäger ligands by introducing seven new variants with diverse substituent combinations (Scheme 1, right), including methyl and phenyl ketones, ethyl esters, and electron-withdrawing nitriles and trifluoromethyl ketone groups. The impact of the asymmetric substitution on the optical, redox, and SCO properties of the ligands and resulting iron(II) complexes was investigated extensively and compared to their symmetrical counterparts. The experimental findings were further supported by DFT calculations. Characterization included single-crystal X-ray diffraction (SC-XRD), NMR, UV–vis spectroscopy, cyclic voltammetry (CV), and magnetic measurements using SQUID magnetometry.

2. Results and Discussion

2.1. Ligand Syntheses

The synthetic route for the asymmetric ligands H_2L^{xy} ($xy = 14$; 15; 16; 25; 26; 34; 56) and their corresponding iron(II) compounds is given in **Scheme 2**. The monosubstituted preligands ${}_{pre}L^{x}$ ($x = 1$, 2, 3, 5) were synthesized via a stoichiometric reaction of *o*-phenylenediamine with the desired keto-enol ether KEE^{x} in EtOH ($x = 1$, 2, 3) or MeOH ($x = 5$).[2,51] adapting established procedures.[50] Subsequent condensation of ${}_{pre}L^{x}$ with a second keto-enol ether KEE^{y} in EtOH afforded the asymmetric ligands with the desired substitution patterns, as previously described for similar systems. Ligands were isolated in moderate to good yields (36–82%) and their identity and purity were confirmed using ^{1}H and ^{13}C NMR spectroscopy (see Figure S1–S14, Supporting Information) as well as CHN elemental analysis.

The most diagnostic signals in ^{1}H NMR spectra arise from the –NH protons, which undergo intramolecular hydrogen bonding with proximal functional groups, typically carbonyl moieties.

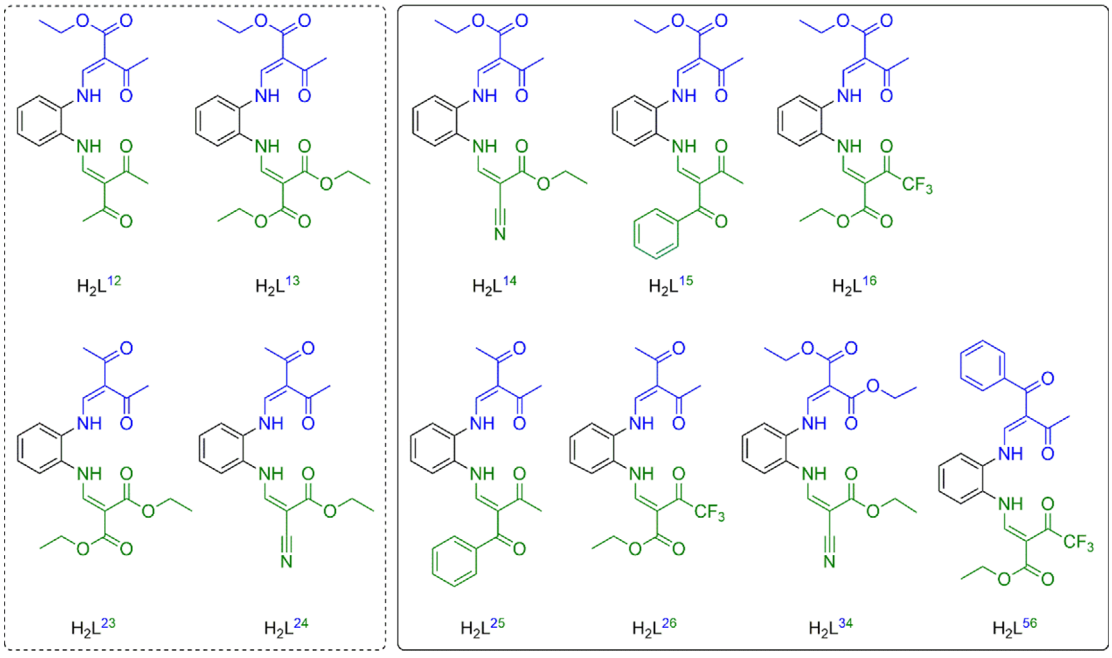

Scheme 1. Overview of previously described (left) and novel (right) asymmetric ligands.

Journal of Inorganic and General Chemistry
ZAAC
Zeitschrift für anorganische und allgemeine Chemie

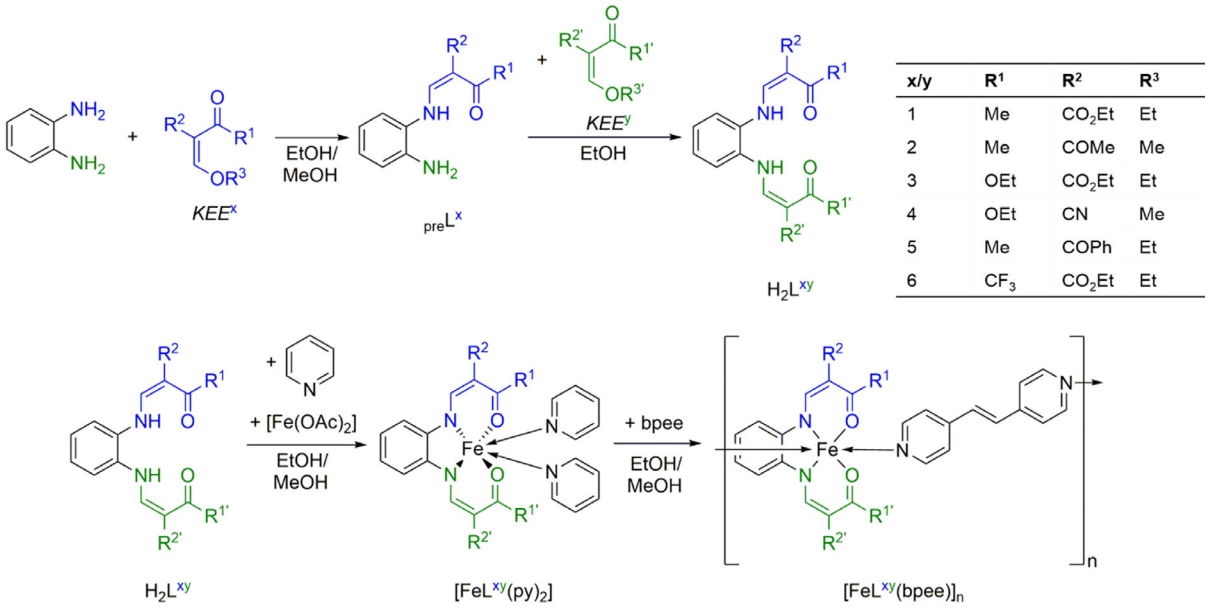

x/y	R¹	R²	R³
1	Me	CO_2Et	Et
2	Me	COMe	Me
3	OEt	CO_2Et	Et
4	OEt	CN	Me
5	Me	COPh	Et
6	CF_3	CO_2Et	Et

Scheme 2. Synthetic procedures for the synthesis of the asymmetric Jäger-ligands and their corresponding iron(II) compounds.

The signal complexity of enamine sections of the ^{1}H NMR spectra between $10 < \delta < 14$ ppm directly reflects the symmetry of the overall ligand, as the enamine units in the ligands exhibit *E/Z* isomerism around the (partial) C═N double bond. Only when both substituents of an enamine function are identical ($x/y = 2$ or 3) and an overall C_{2v}-symmetric ligand is used ($x = y$), a single signal set prevails, due to the presence of a single isomer. Accordingly, for $x/y = 2$ or $x/y = 3$, only a single –NH signal is observed at 12.6 or 10.6 ppm, respectively, pointing to a steering effect of the carbonyl nature on the shift of the enamine proton. By contrast, nonidentical enamine moieties with $x \neq y$ at the enamine positions ($x/y = 1$, 4, 5, 6), allow both enamine moieties to independently adopt *E* or *Z* configurations, resulting in up to four isomers (*EE, EZ, ZE, ZZ*). These isomers all give rise to individual ^{1}H NMR signal sets, prone to overlap. The signal multiplexing due to the presence of isomers is also reflected in the ^{13}C NMR spectra.

For $x = y = 1$, for instance, two –NH signals are observed at 12.5 and 10.6 ppm, corresponding to the –NH hydrogen bonding with the methyl-ketone and ethyl-ester carbonyls, respectively. As is shown below, such differences in the NMR shifts correlate with the H-bond metrics varying with the nature of the carbonyl moiety (see below). Low-field shifted N—H resonances indicate stronger H-bonding and vise versa. Accordingly, the methyl ketone of $x/y = 1$ supports stronger H-bonding than the ester carbonyl; similar distinctions hold true for all other ligands. As the H-bonding acceptor strength of the carbonyl is a measure for the Lewis-basicity of the O-donor site of L^{xy}, this differentiation is highly relevant for the coordination chemistry of the ligands.

The signal intensity of the signal subsets of the isomers mirrors the relative population of the isomers in solution. It favors methyl-ketone H-binding over ester-carbonyl binding with a 6:1 ratio. In the case of $x/y = 6$, that is, with an ester-trifluoromethylketone competition, the –NH signals appear at 12.0 and 11.1 ppm with a smaller intensity ratio of 2:1, attributed to the trifluoromethyl ketone's reduced hydrogen bond acceptor ability compared to its nonfluorinated analog. For $x/y = 5$, signals at 12.4 and 11.1 ppm correspond to competing H-bonding interactions with methyl and phenyl ketone groups, respectively. Interestingly, the isomeric ratio (6:1) is higher than expected if only H-bond strengths are accounted for. This suggests additional steric factors, such as the bulky phenyl group, favoring peripheral positioning. For $x/y = 4$, only ester-based H-bonding is expected due to the unfavorable directionality of the nitrile; however, multiple –NH signals are observed in both the asymmetrical ligand H_2L^{14} and the symmetrical reference H_2L^{44}. This may be due to the presence of other isomers or slow imine-enamine tautomerization, potentially influenced by stabilizing intramolecular hydrogen bonding.

2.2. X-Ray Crystallography of the Ligands

Crystallographic data of ligands H_2L^{14} and H_2L^{25} are summarized in Table S1, Supporting Information. H_2L^{14} crystallizes in the orthorhombic space group $Pna2_1$ with four molecules per unit cell, while H_2L^{15} crystallizes in the monoclinic space group Pc with two molecules per unit cell. In both cases, the asymmetric unit consists of a single ligand molecule, shown in **Figure 1**. Unlike classical Schiff-base ligands derived from diamines and salicylic aldehyde, such as Salen or Salophen, with a C═N imine moiety, the related Jäger ligands favor the keto-enamine form, especially in the solid state.[10,52,53]

Relevant bond lengths within the chelate rings of H_2L^{14} and H_2L^{25} are listed in **Table 1**. The N—C bonds of the enamine units exhibit partial double bond character, as evidenced by their significantly shorter lengths relative to standard N—C single bonds. The bond lengths and angles associated with intramolecular hydrogen bonding within the ligands are reported in **Table 2**.

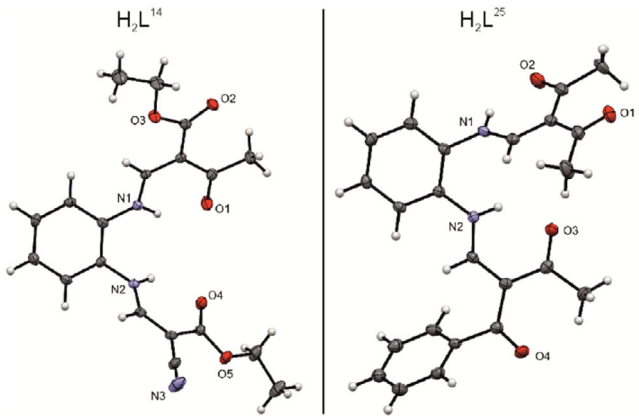

Figure 1. Molecular structures of H_2L^{14} (left) and H_2L^{25} (right) in the crystal. Ellipsoids are drawn at 50% probability.

In the case of H_2L^{25}, a notable disparity is observed: although the ligand features two identical methyl-ketone enamine substituents on the $x = 2$ side, their bond lengths differ more from each other than they do compared to the methyl ketone on the $x = 5$ side. This suggests that hydrogen bonding—both intra- and intermolecular—within the crystal lattice plays a more dominant role in determining bond metrics than the nature of the substituents themselves.

2.3. DFT Modeling of the Ligands

To validate the ketone/ester distinction deduced from NMR chemical shifts and from the solid-state metrics, we performed a DFT study. Some details of the optimized structures of H_2L^{14} and H_2L^{25} are added to Table 1 and 2. DFT data in parentheses compare well with experimental metrics, lending theoretical support to the experimental ketone/ester distinction. That is, the nonbonded N(H)···O distance is longer by >10 pm, when the carbonyl is of the ester type, both in experiment and theory. This consistency motivated a modeling study of the entire ligand series. Pertinent results are depicted graphically in **Figure 2**. As a major result, the ketone/ester distinction holds true in all cases, giving consistently rise to long N(H)···O distances, when esters are involved. This type of loosening of the chelate constraints cannot be referred to effects of the substitution on the bond lengths within the chelate backbone. In fact, the bond lengths in the conjugated chelate arms are hardly affected by the substitution. The distinction can be largely referred to the orientation of the carbonyl C—O bond with respect to the chelate backbone. The inner C—C=O angle of the chelate is very close to the ideal value of 120° for the methyl and phenyl ketones, $x/y = 1$, 2, and 5. When ester-carbonyls or trifluoro methyl ketones are involved, we see a consistent widening of this angle by 3° for $x/y = 3$, 4, and 6, leading to a loosening of the H-bonding. Intriguingly, the above classification of the ligands likewise shines up in the optical absorption behavior in solution.

2.4. Optical Absorption Behavior of the Ligands

UV–vis absorption spectra of all symmetric and asymmetric ligands were measured in MeCN ($c = 1.0 \times 10^{-5}$ M). A representative selection is shown in **Figure 3** with the remaining spectra provided in the Figure S16, Supporting Information. All ligands show two prominent absorption bands in the 270–400 nm range. The absorption spectra of the asymmetric ligands H_2L^{14}, H_2L^{16}, H_2L^{26}, and H_2L^{56} closely resemble an average of their corresponding symmetric references in terms of both peak position and shape, suggesting an additive effect of the substituents. This also applies to the asymmetrical ligands H_2L^{15}, H_2L^{25}, and H_2L^{34}, although in these cases the symmetric parent ligands already feature similar spectra. A third, weaker absorption band is observed in H_2L^{11}, H_2L^{22}, H_2L^{55}, and H_2L^{66} in the range between $\lambda = 220$–270 nm but is absent in H_2L^{33} and H_2L^{44}. Among the asymmetric ligands, only H_2L^{34} does not feature the third absorption band, while in case of H_2L^{14} it appears with significantly reduced

Table 1. Selected bond lengths (Å) within both sides of the chelate rings of H_2L^{14} and H_2L^{25}. Data in parentheses denotes DFT-optimized structures.

Bond	H_2L^{14} ($x = 1$)	H_2L^{14} ($x = 4$)	H_2L^{25} ($x = 2$)[a)]	H_2L^{25} ($x = 5$)
N—C	1.330(3) (1.335)	1.330(3) (1.338)	1.332(4) (1.335)	1.329(3) (1.336)
C=C	1.388(3) (1.398)	1.380(4) (1.392)	1.393(4) (1.401)	1.383(4) (1.398)
C—C	1.460(3) (1.462)	1.448(3) (1.466)	1.473(4)/1.461(4) (1.468)	1.459(4) (1.465)
C=O	1.239(3) (1.262)	1.219(3) (1.239)	1.221(4)/1.243(4) (1.260)	1.236(4) (1.259)

[a)]Bond lengths are given for both methyl ketones.

Table 2. Bond lengths (Å) and angles (°) of intramolecular classical hydrogen bonds of H_2L^{14} and H_2L^{25}. D···A values in parentheses denote DFT-derived data.

Ligand	Bond	D–H	H···A	D···A	D–H···A
H_2L^{14}	N1—H1···O1	0.89(3)	1.82(3)	2.568(3) (2.564)	140(3)
	N2—H2···O4	0.85(5)	2.06(5)	2.695(3) (2.672)	132(4)
H_2L^{25}	N1—H1···O2	0.85(4)	1.94(4)	2.598(3) (2.558)	134(3)
	N2—H2···O3	0.87(4)	1.92(4)	2.607(3) (2.581)	135(3)

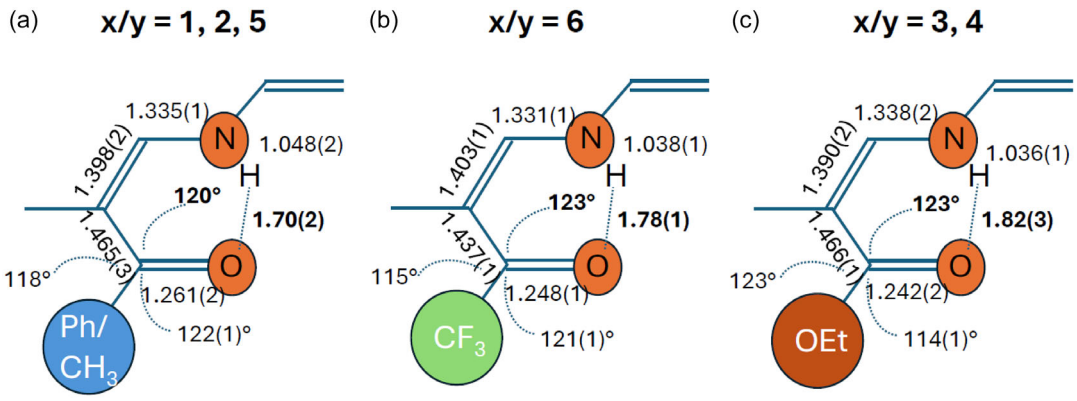

Figure 2. Carbonyl-steered metrics of the H-bonding pattern in the ligands H_2L^{xy}, classified as a) keto carbonyl, b) CF_3 appended carbonyl and c) ester carbonyl.

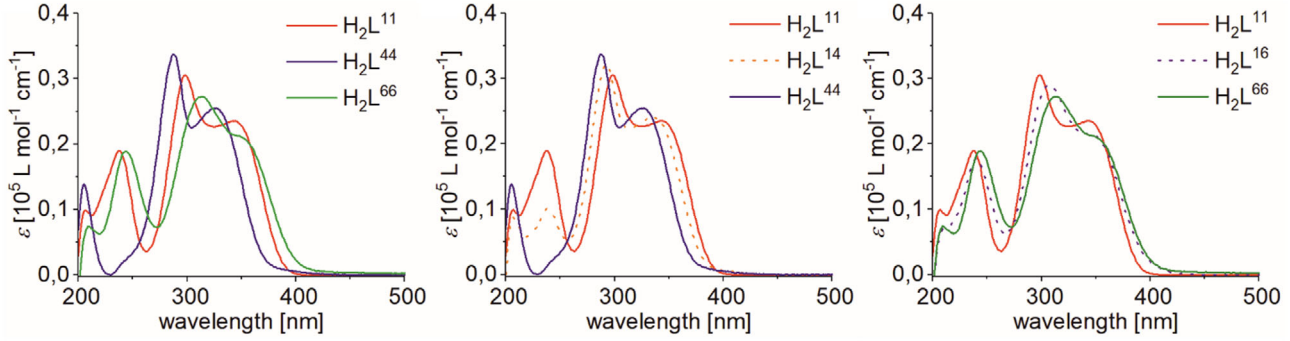

Figure 3. UV–vis absorption spectra of (left) selected symmetric ligands and asymmetric ligands (middle) H_2L^{14} and (right) H_2L^{16} in comparison. Spectra recorded in MeCN ($c = 1.0 \times 10^{-5}$ M).

intensity. These findings indicate that the properties of both ligand sides are additive in solution so that no new effects emerge from asymmetric ligands compared to their symmetric counterparts.

Curiously, the free ligand H_2L^{11} and H_2L^{22} show almost identical absorption behavior at $\lambda > 270$ nm, while H_2L^{33} and H_2L^{44} significantly deviate from them. This implies that even prior to complexation, the lack of a keto-carbonyl group or substitution with only ester and nitrile groups leads to diverging ligand properties. Based on the position and shape of the bands, the ligands can be grouped accordingly.

The first group consists of H_2L^{11}, H_2L^{22}, H_2L^{55}, H_2L^{15}, and H_2L^{25} each displaying two absorption bands at 299 and 346 nm. In all these ligands, it is the keto carbonyl that is (predominantly) involved in intramolecular H-bonding. In agreement with the above classification, the second group consists of H_2L^{33}, H_2L^{44}, and H_2L^{34} with ester-carbonyl oxygen atoms supporting the H-bonding. Here, the leading absorption bands are blue shifted by 860–2270 cm^{-1} relative to group one. By contrast, H_2L^{66} with trifluoromethyl substituted carbonyl exhibits a redshift of 1600 cm^{-1} for the first absorption band, while the second remains largely unchanged.

2.5. Synthesis of Iron(II) Complexes

Iron(II) pyridine complexes were synthesized by reacting the ligands with $[Fe(OAc)_2]$ in pyridine/EtOH (for H_2L^{14}, H_2L^{15}, H_2L^{16}, H_2L^{25}, H_2L^{34}) or pyridine/MeOH (for H_2L^{26}, H_2L^{56}) under inert conditions. Pyridine's stronger donating ability rendered the resulting iron(II) complexes more resistant to oxidation than their methanol or ethanol analogs. For $[FeL^{15}(py)_2]$ and $[FeL^{16}(py)_2]$ the addition of water was necessary to reduce complex solubility and facilitate crystallization. However, attempts to isolate $[FeL^{14}(py)_2]$ via this route were unsuccessful; instead, the less soluble ethanol complex $[FeL^{14}(EtOH)_2]$ was obtained by conducting the reaction solely in EtOH, while the pyridine complex remained elusive in this single case. Furthermore, these iron(II) complexes were employed as building blocks for coordination polymers by reaction with 1,2-bis(4-pyridyl)ethane (bpee) in EtOH (for H_2L^{14}, H_2L^{15}, H_2L^{16}, H_2L^{25}, H_2L^{34}) or MeOH (for H_2L^{26}, H_2L^{56}). The identity and purity of all complexes were confirmed by CHN elemental analysis. It is noted that all compounds, mononuclear complexes and coordination polymers, were obtained without lattice solvation.

2.6. X-Ray Crystallography of Iron(II) Complexes—Molecular Structure

SC-XRD data were obtained for the iron(II) complexes $[FeL^{15}(py)_2]$, $[FeL^{16}(py)_2]$, $[FeL^{34}(py)_2]$, and $[FeL^{56}(py)_2]$. Suitable crystals of $[FeL^{15}(py)_2]$ and $[FeL^{34}(py)_2]$ were obtained from the filtrates of reaction mixtures after prolonged storage at room temperature.

Crystals of $[FeL^{16}(py)_2]$ and $[FeL^{56}(py)_2]$ were taken directly from the isolated product.

Data were collected at 120 K for $[FeL^{15}(py)_2]$, $[FeL^{16}(py)_2]$, and $[FeL^{34}(py)_2]$, while additional data for $[FeL^{16}(py)_2]$ were also collected at 250 K. $[FeL^{56}(py)_2]$ was measured at 170 K. A summary of the crystallographic parameters is given in Table S2, Supporting Information. All complexes crystallized solvent-free. Due to poor data quality, the structure of $[FeL^{56}(py)_2]$ is used solely to confirm the molecular connectivity and the spin state of the iron center. The asymmetric units of $[FeL^{15}(py)_2]$, $[FeL^{16}(py)_2]$, and $[FeL^{34}(py)_2]$ are displayed in **Figure 4**. The asymmetric unit of $[FeL^{56}(py)_2]$ is given in Figure S15, Supporting Information.

As expected, for all complexes the iron(II) centers adopt an octahedral N_4O_2 coordination environment, consisting of two axial pyridine ligands and the equatorial tetradentate Jäger ligand. The spin states were derived from Fe—N/O bond lengths and O_{eq}–Fe–O_{eq} bite angles and additionally confirmed by DFT modeling of the spin-state dependent structures. Selected bond distances and angles from SC-XRD and DFT are provided in **Table 3**. We find excellent agreement between experimental and theoretical data. A more extensive summary of DFT-derived metrics is provided in Figure S19, Supporting Information.

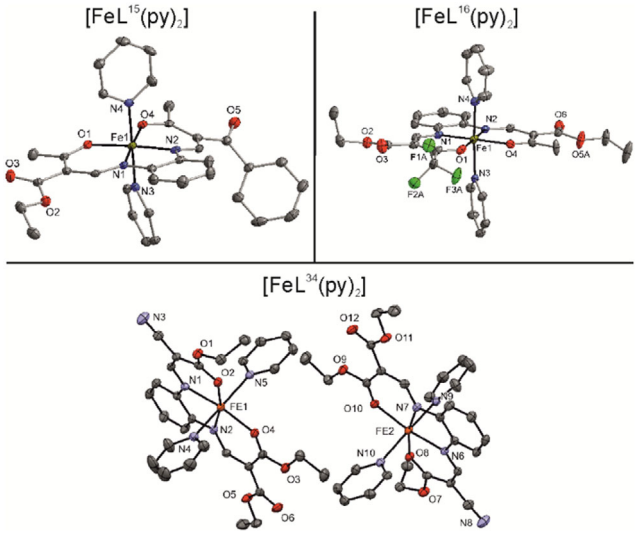

Figure 4. Structure of the asymmetric units in $[FeL^{15}(py)_2]$, $[FeL^{16}(py)_2]$, and $[FeL^{34}(py)_2]$. Hydrogen atoms are omitted for clarity. Ellipsoids are drawn at 50% probability.

Complexes $[FeL^{15}(py)_2]$ and $[FeL^{16}(py)_2]$ exhibit short M—L bonds and bite angles around 90°, consistent with the low-spin (LS) state at 120 K and in agreement with magnetic susceptibility measurements (see below).[9,54] Interestingly, for $[FeL^{16}(py)_2]$, no significant structural changes are observed between 120 and 250 K, indicating persistent LS character. Given the magnetic data showing a SCO at $T_{1/2} = 196$ K, this discrepancy may be attributed to the presence of multiple polymorphic phases. The crystallized polymorph appears to remain LS beyond 250 K. Notably, the two axial pyridine ligands in $[FeL^{15}(py)_2]$ are nearly orthogonal (torsion angle ≈ 85°), whereas in the other complexes the pyridine planes are usually parallel (torsion angles ≤18°), which reflects differences in packing due to steric interactions. It is noted that in a related setting we could recently trace the kinetic peculiarities of (anti) cooperative SCO to the relative orientation of axial pyridine ligands.[10]

In contrast, the bond lengths and angles in $[FeL^{34}(py)_2]$ are typical for the HS state and align with magnetic data, which indicated a conserved HS state even at lowest temperatures. Although the precision of the structural data for $[FeL^{56}(py)_2]$ is limited, the observed bond lengths suggest an HS configuration at 170 K, consistent with its incomplete spin transition starting only below 130 K.

Overall, we conclude that the Fe—O and Fe—N_{eq} bond lengths and the O—Fe—O angle largely reflect the spin state of the complex in the field of asymmetric ligands. As consistently seen in previous related studies with symmetric ligands, the large spin-state driven variation by ≈0.1 Å of the former and ≈20° of the latter allows a safe assignment of the spin state. Despite the limited size of the data set, however, the metrics of the inner coordination sphere of the solid-state structures allow one additional important conclusion to be made. While both being in their HS states, $[FeL^{56}(py)_2]$ and $[FeL^{34}(py)_2]$ differ massively with

Table 3. Selected bond lengths (Å) and angles (°) in the solid-state structures of $[FeL^{15}(py)_2]$, $[FeL^{16}(py)_2]$, $[FeL^{34}(py)_2]$, and $[FeL^{56}(py)_2]$. Data in parentheses refers to DFT-optimized structures of ls-$[FeL^{15}(py)_2]$, ls-$[FeL^{16}(py)_2]$, hs-$[FeL^{34}(py)_2]$, and hs-$[FeL^{56}(py)_2]$.

	$[FeL^{15}(py)_2]$	$[FeL^{16}(py)_2]$	$[FeL^{16}(py)_2]$	$[FeL^{34}(py)_2]$	$[FeL^{34}(py)_2]$	$[FeL^{56}(py)_2]$[a]
				120 K	120K	
T [K]	120 K	120 K	250 K	Complex 1	Complex 2	170 K
d(Fe–O_{eq})	1.932(2) (1.936)	1.9312(15) (1.931)	1.9323(18)	2.0864(12) (2.074)	2.0909(12)	2.01 (2.011)
	1.942(2) (1.943)	1.9379(14) (1.938)	1.9386(18)	2.0590(12) (2.050)	2.0761(12)	2.04 (2.013)
d(Fe–N_{eq})	1.892(3) (1.894)	1.8966(17) (1.896)	1.904(2)	2.1087(14) (2.095)	2.1142(14)	2.09 (2.076)
	1.893(2) (1.889)	1.8948(17) (1.893)	1.898(2)	2.0894(14) (2.081)	2.0929(14)	2.09 (2.077)
d(Fe–N_{ax})	1.994(2) (1.952)	2.0033(17) (1.987)	2.008(2)	2.2508(15) (2.240)	2.2612(15)	2.21 (2.179)
	2.001(2) (1.978)	1.9976(18) (1.957)	2.005(2)	2.2268(14) (2.151)	2.2279(15)	2.27 (2.248)
∡(O_{eq}–Fe–O_{eq})	89.15(9) (87.2)	88.11(6) (86.8)	88.69(8)	106.28(5) (109.5)	106.67(5)	112 (108.9)
∡(N_{ax}–Fe–N_{ax})	175.90(11) (178.3)	174.20(7) (178.1)	174.23(8)	170.35(5) (176.3)	170.52(5)	173 (178.1)
py–py-torsion	86.0	7.3	5.0	18.1	1.7	1

[a]Measured values are approximate; estimated standard deviations are not given due to the data quality.

respect to their Fe—O bond lengths. Keto-carbonyl coordination with $x/y = 5, 6$ leads to stronger Fe—O bonds which are shorter by ≈6 pm than their ester congeners with $x/y = 3, 4$. This distinction had been observed previously in a study on symmetric ligands with $x = y$, highlighting consistently longer Fe—O bonds in the case of ester- carbonyl coordination. In fact, a DFT survey of the entire complex series fully confirms this difference (see Figure S19, Supporting Information). This distinction also echoes the distinction made among the neat ligands in the above. It is tempting to associate the striking preference of ester-coordinate iron(II) for the HS state to the steric peculiarities, namely the directionality of the carbonyl C—O bond.

2.7. Computation of SCO Energies

Linear plots of the apparent SCO energies obtained in a Fock-exchange scan via variation of the exact exchange a_0 in the B3LYP functional (Equation 1)[55,56] allow to study the impact of the substitution pattern on the SCO energies. Within a family of complexes, the slopes are typically identical, so that the offset of the plots will reflect the impact of the substitution pattern on the SCO energies. These routines proved valuable in several preceding studies.[10,57–59] Such-way derived plots are shown in **Figure 5**, the results of the linear regression can be found in **Table 4**.

$$\Delta_{SCO}E = \Delta_{SCO}E^0 + (\delta_{SCO}E \times a_0) \quad (1)$$

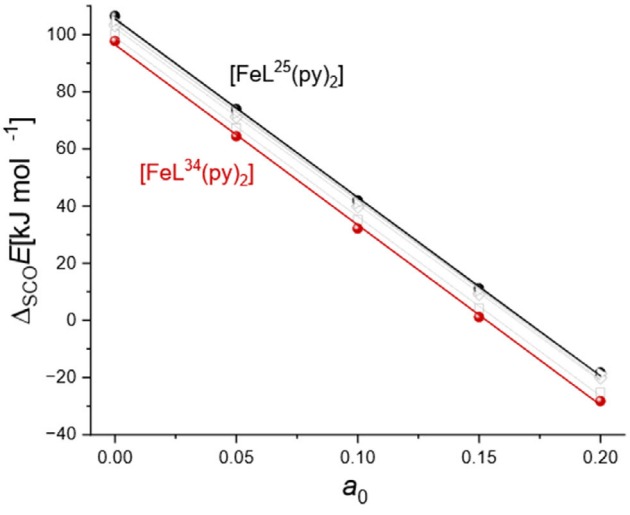

Figure 5. DFT-derived (B3LYP-D/TZVP) apparent SCO energies of complexes [FeL$^{x/y}$(py)$_2$] as a function of the amount of exact Fock-exchange a_0. Highlighted are the complexes with maximum (black) and minimum (red) y-intercepts.

$\Delta_{SCO}E$ denotes the DFT-derived difference of electronic energies of LS and HS, that is, $\Delta_{SCO}E = E(\text{HS}) - E(\text{LS})$. Positive values of $\Delta_{SCO}E$ denote a preference of LS. $\Delta_{SCO}S$ denotes the thermodynamic difference of entropies of LS and HS, that is $\Delta_{SCO}S = S(\text{HS}) - S(\text{LS})$. For iron(II) complexes the values of $\Delta_{SCO}S$ are typically positive, implying an entropy driven preference of HS at elevated temperature. As seen previously within the symmetric complexes [FeL$^{x/y}$(py)$_2$] with $x = y$, also the asymmetric ones join the complex family. The slopes hardly differ from the previously described symmetric complexes, giving almost identical values of $\delta_{SCO}E = -(625 \pm 8)$ kJ mol^{-1}. Despite the narrow crowding, the smallest slopes are consistently found for complexes with trifluoromethyl substituents, deriving from H_2L^{16}, H_2L^{66}, H_2L^{66}, and H_2L^{66}, whereas the largest slopes apply to complex with ester-carbonyl coordination, deriving from H_2L^{33}, H_2L^{34}, and H_2L^{44}. It is noted that H_2L^{14} does not fit into this grouping, indicating a dominating influence of the keto carbonyl for $x = 1$. Given the parallel course of the plots, the vertical ordering reports on the relative SCO energies in a direct way: the smaller the y-intercept, the larger the SCO energy. Reasonably assuming invariant SCO entropies of $\Delta_{SCO}S = 80$ J K^{-1} mol^{-1}, the variation in y-intercepts of ≈10 kJ mol^{-1} lets us expect a variation range of molecular SCO transition temperatures, $\Delta T_{1/2} \approx 120$ K across the asymmetric series. This span should be compared with the slightly larger one reported for the symmetric congeners, that is, $\Delta\Delta_{SCO}E = 14$ kJ mol^{-1} and $\Delta T_{1/2} \approx 170$ K.[38]

The intercepts of the asymmetric complexes can be well predicted through interpolation of the respective symmetric complexes; only for [FeL^{26}(py)$_2$] the predicted value deviates by more than 1 kJ mol^{-1}. This consistency gives additional support to the idea of additive electronic effects of the enamine substituents.

2.8. Redox Behavior of the Iron(II) Complexes

Electrochemical data of several symmetric members of the complex series have been reported previously.[60,61] To create a consistent data set, CV measurements were performed for the complete series of symmetric and asymmetric iron(II) pyridine complexes in pyridine, using (n-Bu$_4$N)(PF$_6$) ($c = 0.1$ M) as the supporting electrolyte and a reversible hydrogen reference electrode (RHE) as the reference (scan rates of 50, 100, 500, and 1000 mV s^{-1}). The cyclic voltammograms of the complete set of symmetric and asymmetric complexes are depicted against the ferrocenium/ferrocene (Fc$^+$/Fc) redox couple in Figure S22 and S23, Supporting Information and the corresponding electrochemical parameters are given in Table S6, Supporting Information. The results discussed in the following leave no doubt that the electrochemical parameters of the asymmetric complexes can be reliably interpolated from the symmetric parent

Table 4. Fitting results of the linear regressions for complexes [FeL$^{x/y}$(py)$_2$]; energies in kJ mol^{-1}.

X =	L^{14}	L^{15}	L^{16}	L^{25}	L^{26}	L^{34}	L^{56}
$\delta_{SCO}E$	−628(8)	−628(7)	−617(6)	−625(7)	−617(6)	−631(9)	−617(7)
$\Delta_{SCO}E^0$	99(1)	105(1)	104(1)	106(1)	102(1)	96(1)	104(1)
R^2	0.9994	0.9995	0.9995	0.9995	0.9996	0.9992	0.9995

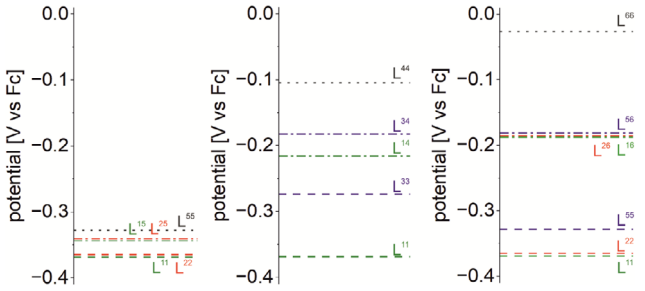

Figure 6. Measured $E_{1/2}$ of iron(II) pyridine complexes with symmetric and asymmetric ligands with certain functional groups: (left) phenyl ketone, (middle) trifluoromethyl ketone, and (right) nitrile.

complexes, as illustrated in **Figure 6**. Different from the above discussion, however, the electrochemical data cannot be classified along the ester/ketone divide.

Out of the symmetric reference complexes only $[FeL^{11}(py)_2]$, $[FeL^{22}(py)_2]$, and $[FeL^{55}(py)_2]$ showed a fully reversible $Fe^{3+/2+}$ redox event. In $[FeL^{33}(py)_2]$ the iron oxidation is quasireversible, while $[FeL^{44}(py)_2]$ and $[FeL^{66}(py)_2]$ show poor reversibility, likely due to follow-up reactions of the iron(III) species. The measured half wave potential $E_{1/2}$ for the $Fe^{3+/2+}$ redox couple is nearly identical (−0.37 V) for $[FeL^{11}(py)_2]$ and $[FeL^{22}(py)_2]$, while $[FeL^{33}(py)_2]$ and $[FeL^{55}(py)_2]$ display anodic shifts of $\approx\Delta E_{1/2} = +90$ mV and +40 mV respectively. Substantially larger anodic shifts are observed for $[FeL^{44}(py)_2]$ and $[FeL^{66}(py)_2]$, with $\Delta E_{1/2} = +260$ mV and 310 mV, respectively. These stark shifts reflect the presence of the strong electron-withdrawing nitrile and trifluoromethyl groups, which stabilize the iron(II) oxidation state and thus increase the oxidation potential. The particularly strong impact of trifluoromethyl groups has been previously identified in π-extended analogs of $[FeL^{66}(py)_2]$.[28] In contrast, the minor shift observed in $[FeL^{33}(py)_2]$ is likely due to mesomeric effects of the coordinating ester group.

Regarding the reversibility of the iron-borne oxidation events, a stabilization of the iron(II) oxidation state seems to correlate with reduced reversibility. Notably, while $[FeL^{44}(py)_2]$ shows the lowest degree of redox reversibility, $[FeL^{66}(py)_2]$ realizes the greatest stabilization of the iron(II) state, as indicated by the most anodically shifted E^{ox} and $E_{1/2}$ values. This is likely due to the coordination of $[FeL^{44}(py)_2]$ through an ester-carbonyl, which also reduces reversibility by promoting follow up reactions. This agrees with $[FeL^{33}(py)_2]$ also showing reduced reversibility.

The novel asymmetric complexes display electrochemical behavior largely comparable to their symmetrical counterparts, both in terms of reversibility and observed redox potential. For asymmetric complexes bearing electron-withdrawing groups, the observed $E_{1/2}$ values deviate by only ≈10 mV from the average of their two symmetrical counterparts, as visualized in Figure 6. This correlation of additive substitution effects also applies for $[FeL^{15}(py)_2]$ and $[FeL^{25}(py)_2]$, even though the effect of their functional groups on $E_{1/2}$ is rather small in comparison. These findings support the predictable fine-tuning of redox potentials via ligand substitution, which further enables the design of redox-active materials with tailored electronic properties.

2.9. UV–vis Spectra of the Iron(II) Complexes

Different from the ligand spectra (see Figure 3), the UV–vis absorption spectra of the symmetric and asymmetric pyridine complexes were recorded in pyridine ($c = 2.0 \times 10^{-5}$ M). This difference acknowledges the coordination potential of MeCN, which would render competitive MeCN and pyridine coordination. Since pyridine strongly absorbs at wavelengths <300 nm, the spectra were measured only above this range; in fact, discontinuous spectra "jumps" due to nonperfect background subtraction are evident already at $\lambda = 320$ nm. Due to the failure to receive bulk $[FeL^{14}(py)_2]$ synthetically, it was generated in situ from $[FeL^{14}(EtOH)_2]$ through spontaneous ligand exchange. Representative spectra are shown in **Figure 7**, with the remaining spectra provided in Figure S17, Supporting Information. To better illustrate the low-energy tailing with lower relative absorbance, the data are additionally presented on a logarithmic scale in the Figure S18, Supporting Information.

As a first important finding, all complex spectra echo shape and intensity distribution of the respective ligand spectra up to ≈400 nm, if somewhat bathochromically shifted. That is, a first absorption band is found between 310 and 345 nm, two overlapping ones between 350 and 420 nm and a third, broad absorption band at $\lambda > 450$ nm which extends up to ≈600 nm in some cases. As can be seen from a comparison of asymmetric complexes with the symmetric parents in Figure 7, the position of these weak bands is significantly affected by the nature of the enamine substituent. Given the low intensity of the latter, these are tentatively assigned as d–d transitions of the iron(II) center. This assignment agrees with time dependent-DFT (TD-DFT) calculations (see below).

The qualitative classification made for the free ligands largely persists in the complexes. Keto-coordinate $[FeL^{11}(py)_2]$, $[FeL^{22}(py)_2]$, $[FeL^{55}(py)_2]$, $[FeL^{15}(py)_2]$, and $[FeL^{25}(py)_2]$ all show very similar absorption spectra. In contrast, $[FeL^{33}(py)_2]$ and $[FeL^{44}(py)_2]$ with coordinated ester carbonyls display a consistent blueshift across all bands. Again, in agreement with the ligand spectra, $[FeL^{66}(py)_2]$ shows a redshift. Although the degree of shift varies between bands, the direction of the shift seems to be consistent, even applying to the long-wavelength tailing. For instance, the absorption spectrum of $[FeL^{14}(py)_2]$ is the average of the spectra observed for its symmetric references $[FeL^{11}(py)_2]$ and $[FeL^{44}(py)_2]$. $[FeL^{34}(py)_2]$ aligns broadly with $[FeL^{33}(py)_2]$ and $[FeL^{44}(py)_2]$, albeit with slight deviations.

However, an interpolation between the parent spectra is not successful in all cases, indicating (partial) nonadditivity of the UV–vis spectroscopic response. In particular, the low-energy tailing of $[FeL^{16}(py)_2]$, $[FeL^{26}(py)_2]$, and $[FeL^{56}(py)_2]$ match more closely with $[FeL^{66}(py)_2]$ than with their other symmetric references $[FeL^{11}(py)_2]$, $[FeL^{22}(py)_2]$, and $[FeL^{55}(py)_2]$, respectively (see Figure S18, Supporting Information). The influence of the trifluoromethyl substituent at the coordinated ketone outcompetes the effects of the alkyl and phenyl substituents. This behavior contrasts with that of the free ligands, where absorption spectra were generally additive. Here the $x = 6$ substituent seems to dictate the absorption properties, even in asymmetric complexes. The results indicate that one-sided substitution with $x = 6$ does have

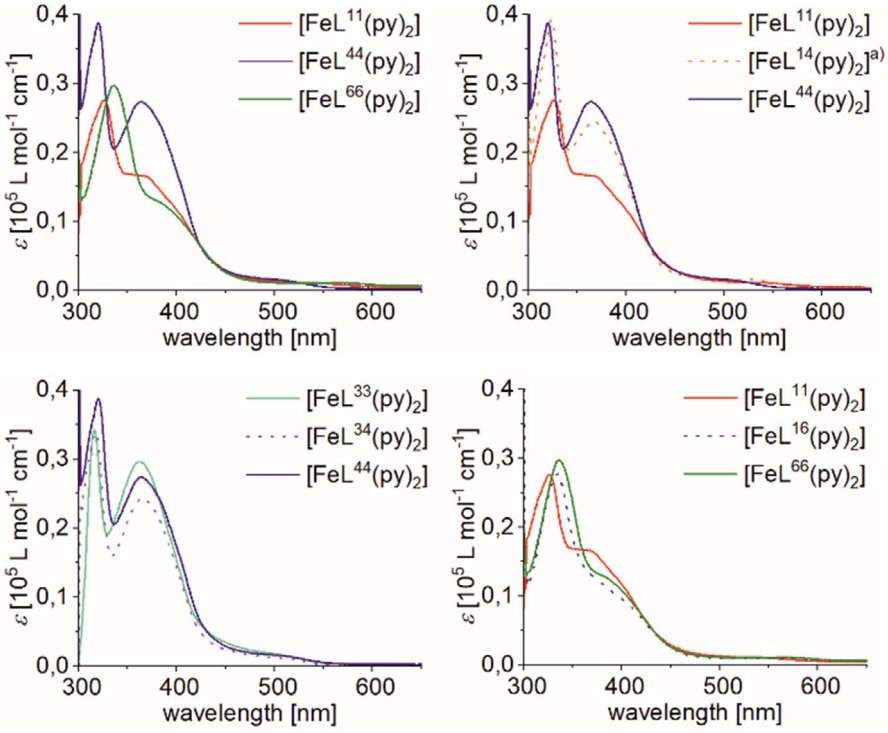

Figure 7. UV–vis absorption spectra of (left) selected symmetrical complexes as well as asymmetrical complexes (middle) $[FeL^{14}(py)_2]$ and (right) $[FeL^{16}(py)_2]$ in comparison. Spectra recorded in pyridine ($c = 2.0 \times 10^{-5}$ M). a) $[FeL^{14}(py)_2]$ was generated in situ from its corresponding EtOH-complex.

a similarly strong influence on the complex's absorption spectrum as the two-sided substitution for $x = y = 6$.

2.10. TD-DFT-Derived Spectra of the Iron(II) Complexes

The optical spectra of the asymmetric complexes $[FeL^{x/y}(py)_2]$ ($x \neq y$) in their HS states were modeled with TD-DFT methods using the TPSSh hybrid functional. These settings gave excellent agreement with experiment in several previous studies on 3d-metal complexes.[27,62,63] In keeping with this, the experimental transition energy and intensity could be satisfyingly matched for all complexes in this study (c.f., **Figure 8** for three selected examples; for more spectra see the ESI, Figure S20, Supporting Information).

As stated above, the broad near UV transition envelope between 300–400 nm is largely conserved upon coordination to iron(II), if slightly red-shifted. This consistency indicates ligand-borne transitions to be responsible. Indeed, TD-DFT shows that they are a convolute of numerous individual transitions of varying character; nevertheless, the dominating transitions possess sharply decreased metal character and utilize donor orbitals located on the conjugated ligand backbone, rendering the transition(s) intraligand charge transfer (ILCT) like. Inspection of the transition densities of the leading UV transitions supports this assignment as $\pi\pi^*$ excitations with only marginal contribution of the metal (see Figure S21, Supporting Information). Similar conclusions and assignments hold for all complexes.

By contrast, the broad and rather weak vis bands in the experimental spectrum of $[FeL^{14}(py)_2]$, $[FeL^{16}(py)_2]$, and $[FeL^{34}(py)_2]$ at $\lambda > 400$ do not find a counterpart in the ligand spectra. They are clearly metal borne. Difference densities of these transitions indicate a dominating dd-like character with the CT character increasing with wavelength. It is noted that the mixed dd/CT transitions which occur at $550\,\text{nm} < \lambda < 600\,\text{nm}$ in all compounds, do not match the experimental spectra. This deviation is likely due to DFT-inherent problems of adequately treating CT states.[64]

2.11. X-Ray Crystallography of Iron(II) Complexes—Packing

$[FeL^{15}(py)_2]$ crystallizes in the monoclinic space group $P2_1/c$ with one complex molecule per asymmetric unit (see Figure 4). Both $[FeL^{16}(py)_2]$ and $[FeL^{34}(py)_2]$ crystallize in the triclinic space group $P\,\bar{1}$, with one and two molecules per asymmetric unit, respectively. $[FeL^{56}(py)_2]$ crystallizes in the orthorhombic space group $P2_12_12_1$. The structure contains one complex molecule per asymmetric unit (Figure S15, Supporting Information). The limited access to reference crystal data does not allow a comprehensive discussion of the (non) additive effects of ligand asymmetry on the overall packing. It is noted, however, that the symmetric reference complexes $[FeL^{11}(py)_2]$, $[FeL^{22}(py)_2]$, $[FeL^{33}(py)_2]$, and $[FeL^{66}(py)_2]$ all crystallize in monoclinic space group $P2_1/c$,[65,66] as does also the asymmetric complex $[FeL^{15}(py)_2]$. Unfortunately, no crystal structure has been reported for $[FeL^{55}(py)_2]$, and only related structures with different axial ligands are available, limiting meaningful structural comparisons due to expected packing variations. Comparison of triclinic $[FeL^{34}(py)_2]$ with the symmetric parent compounds is likewise hampered. While neat $[FeL^{33}(py)_2]$

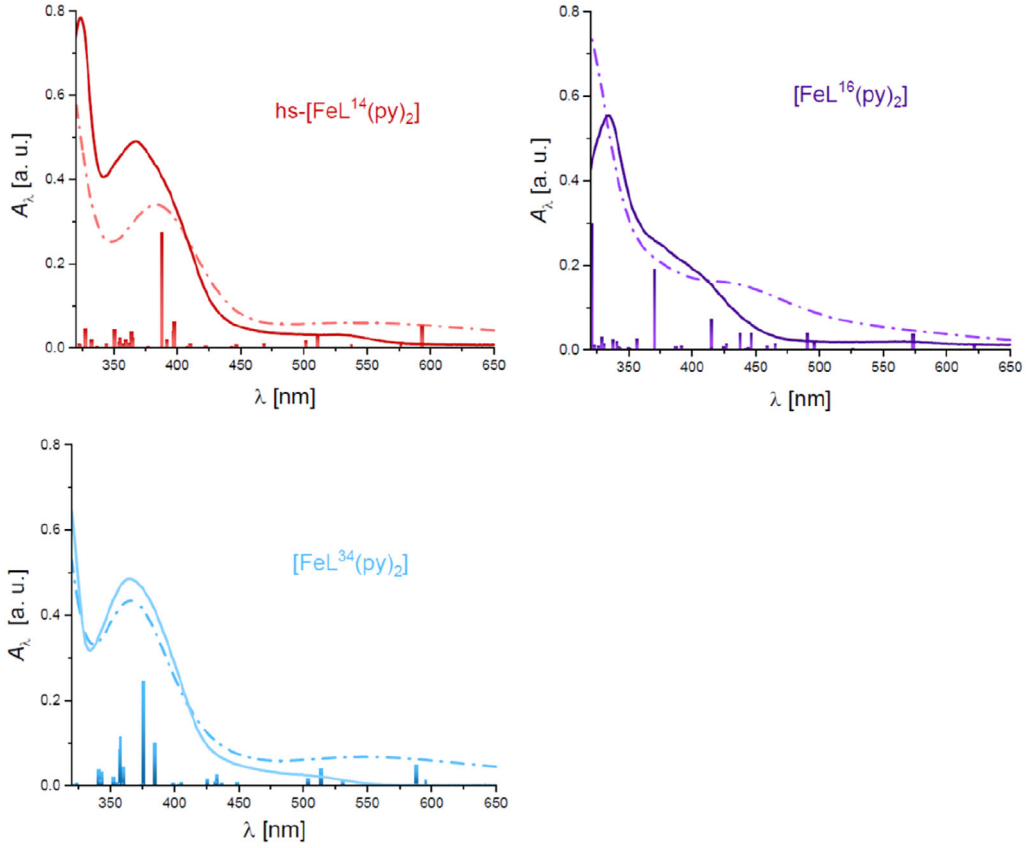

Figure 8. DFT modeling of the experimental UV–vis spectra of UV–vis absorption spectra of $[FeL^{14}(py)_2]$ (left), $[FeL^{16}(py)_2]$ (middle), and $[FeL^{34}(py)_2]$ (right). Experimental data (replotted on from Figure 7) and DFT spectra are given as continuous and broken lines, respectively. Theoretical spectra were computed from the vertical line spectra through appropriate broadening.

has a monoclinic packing, it is noted that monoclinic $[FeL^{44}(py)_2]$ so far only afforded with cocrystallized pyridine, complicating direct comparison.[36]

In solid-state SCO compounds, cooperativity between metal centers—largely mediated by intermolecular interactions—is critical for abrupt transitions and hysteresis. Both $[FeL^{15}(py)_2]$ and $[FeL^{16}(py)_2]$ display gradual SCO behavior in SQUID measurements. This does not necessarily imply low cooperativity in the single crystal; rather, the polycrystalline nature of bulk samples may obscure sharper transitions. Crystal packing in $[FeL^{15}(py)_2]$, $[FeL^{16}(py)_2]$, and $[FeL^{34}(py)_2]$ is dominated by nonclassical hydrogen bonding involving C—H···O/N interactions.

In $[FeL^{15}(py)_2]$, all hydrogen bonds involve carbonyl oxygen atoms as acceptors (Table S3, Supporting Information). The ester-carbonyl participates in two hydrogen bonds (one with an ethyl H and one with a pyridine H) while the phenyl ketone also forms a hydrogen bond with a pyridine H. Additionally, the two chelate oxygen atoms accept hydrogen bonds from pyridine H atoms, generating column-like structures in [010] direction (**Figure 9**).

In $[FeL^{16}(py)_2]$, two types of positional disorder are observed in the ligand periphery. First, the substituents on both sides of the ligand core are flipped with an occupancy ratio of 0.664(2):0.336(2). This disorder arises from the symmetry between the identical ethyl-ester groups and the similar steric bulk of the methyl (CH_3) and trifluoromethyl (CF_3) substituents. Second, one ethoxy group on the ligand exhibits conformational disorder with an occupancy of 0.80(2):0.20(2), reflecting rotational flexibility. Especially the first of these disorders influences crystal packing and interactions. The proximity of CF_3 groups in neighboring disordered sites enables short F···F contacts, as shown in **Figure 10** (right). The overall crystal packing displays parallel alignment of all Jäger ligand chelate planes (Figure 10, left), which may be stabilized by these noncovalent F···F as well as C—H···O interactions (see Table S4, Supporting Information).

In $[FeL^{34}(py)_2]$, nonclassical hydrogen bonding involves both oxygen and nitrogen acceptors. Notably, the nitrile substituents enable C—H···N interactions in addition to the typical C—H···O contacts. These interactions organize the crystal packing into a 2D hydrogen-bonded network in the [101] plane, while no significant interactions are observed along the [010] direction (**Figure 11** and Table S5, Supporting Information). The cooperative network is limited to a single plane, which may influence the SCO behavior by reducing 3D cooperativity. However, we feel that molecular metrics are more important than supramolecular aspects in this special case. Indeed, the distinction between "keto-ligands" with $x/y = 1, 2, 5, 6$ on the one hand and ester ligands $x/y = 3, 4$ on the other persists in the respective complexes.

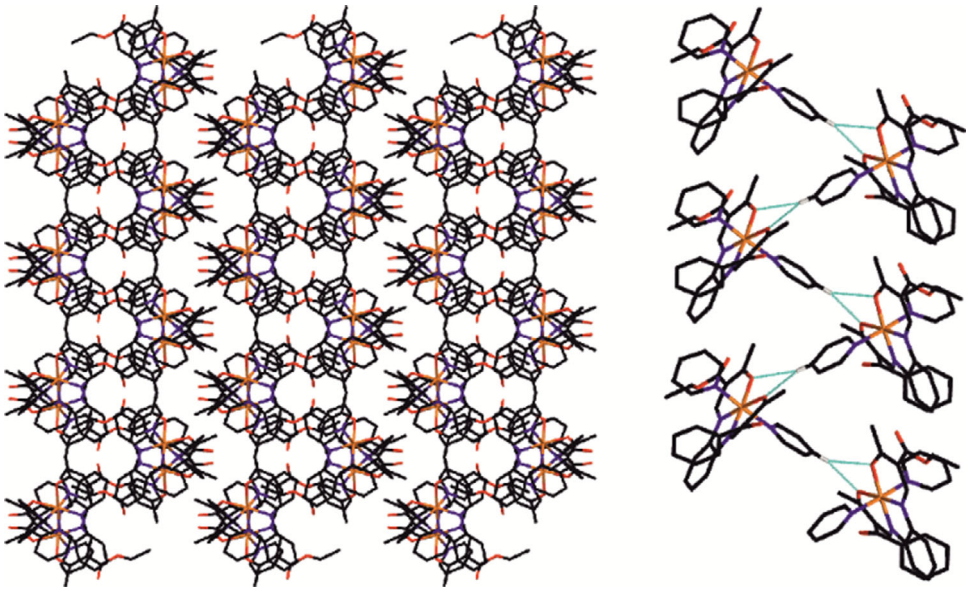

Figure 9. Molecular packing of $[FeL^{15}(py)_2]$ (left) shown along [001]. Hydrogen atoms are omitted for clarity. (right) nonclassical hydrogen bonds between pyridine hydrogen and the two oxygen atoms of the chelate ring.

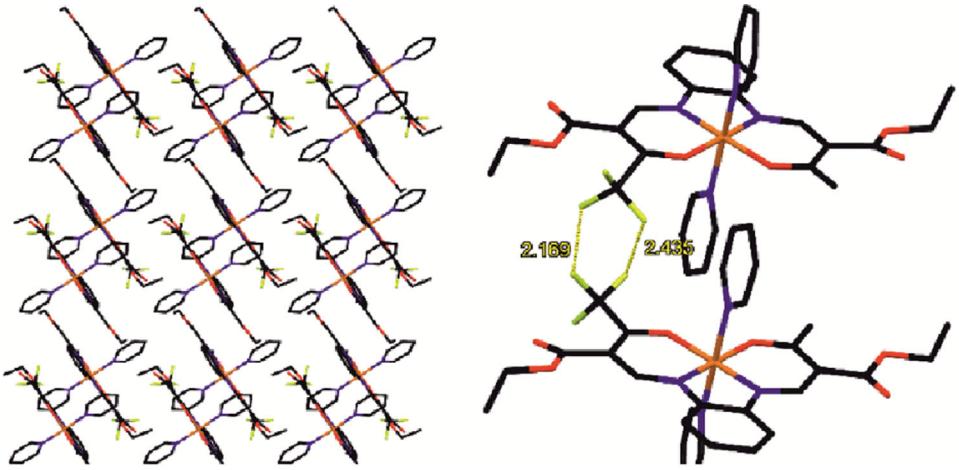

Figure 10. (left) Molecular packing of $[FeL^{16}(py)_2]$ shown along [001]. Hydrogen atoms are omitted for clarity. (right) F—F interactions between two neighboring complex molecules because of disorder.

2.12. Magnetic Properties of Mononuclear Complexes

Temperature-dependent magnetic susceptibility measurements were performed to investigate the spin states of the iron(II) complexes. For the diamagnetic LS state with a $t_{2g}^6e_g^0$ configuration, $\chi_M T$ values of around 0 $cm^3\,K\,mol^{-1}$ are expected. In contrast, for the paramagnetic HS state a $\chi_M T$ product of around 3.5 $cm^3\,K\,mol^{-1}$ are typically observed.[54] All measurements were carried out between 5 and 350 K using a SQUID magnetometer at a scan rate of 5 $K\,min^{-1}$, both in the cooling and in the heating mode.

Symmetric pyridine complexes of H_2L^{11}, H_2L^{22}, H_2L^{55}, and H_2L^{66} have previously been reported to exhibit SCO behavior, both in the solid state and solution, with spin transition temperatures $T_{1/2}$ ranging from 105 to 220 K.[38,54] In contrast, the reference complexes $[FeL^{33}(py)_2]$ and $[FeL^{44}(py)_2]$ remain in the HS state throughout the full temperature range. The $\chi_M T$ versus T plots of the six asymmetric pyridine complexes are presented in **Figure 12**, with $T_{1/2}$ values of their symmetric references indicated for comparison. A summary of the SCO characteristics is provided in **Table 5**.

Even a cursory visit of the data in Figure 12 makes clear that the magnetic behavior of the asymmetric complexes cannot be comprehensively predicted or interpolated from the respective symmetric parent compounds. The transition temperatures of the latter are indicated as vertical lines in Figure 12. Out of the six pyridine complexes, $[FeL^{25}(py)_2]$, $[FeL^{26}(py)_2]$, and $[FeL^{34}(py)_2]$ stay in the HS state through the whole temperature range with $\chi_M T$ values of 3.3–3.5 $cm^3\,K\,mol^{-1}$, with no indication of SCO. This behavior was expected for $[FeL^{34}(py)_2]$, as both of its symmetrical

Journal of Inorganic and General Chemistry
ZAAC
Zeitschrift für anorganische und allgemeine Chemie

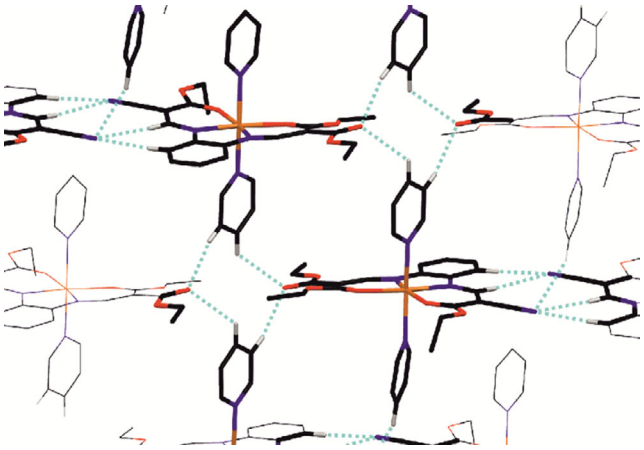

Figure 11. Nonclassical hydrogen bonds of asymmetric unit in $[FeL^{34}(py)_2]$. Hydrogen atoms are omitted for clarity.

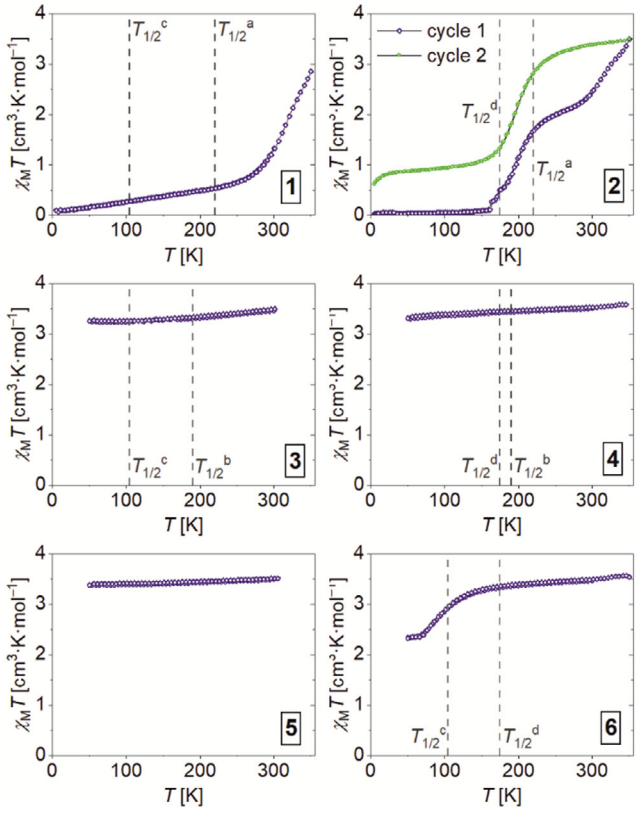

Figure 12. Temperature dependence of $\chi_M T$ of all iron(II) pyridine complexes in varying temperature ranges, measured with a scan rate of 5 K min^{-1} for one or two cycles. 1 $[FeL^{15}(py)_2]$, 2 $[FeL^{16}(py)_2]_n$, 3 $[FeL^{25}(py)_2]$, 4 $[FeL^{26}(py)_2]$, 5 $[FeL^{34}(py)_2]$, 6 $[FeL^{56}(py)_2]$. Verticals indicate the transition temperatures of the related symmetric references: a) $[FeL^{11}(py)_2]$; b) $[FeL^{22}(py)_2]$; c) $[FeL^{55}(py)_2]$; and d) $[FeL^{66}(py)_2]$.

reference ligands also do not support SCO. However, the lack of SCO in $[FeL^{25}(py)_2]$ and $[FeL^{26}(py)_2]$ is clearly unexpected, given that complexes of their reference ligands (H_2L^{22}, H_2L^{55}, H_2L^{66}) all show thermal SCO.

Table 5. SCO behavior in solid of the iron(II) complexes.

	Complex	SCO behavior/spin state	$T_{1/2}$ [K]
Literature	$[FeL^{11}(py)_2]$	Gradual	220
	$[FeL^{22}(py)_2]$	Abrupt, with hysteresis	190
	$[FeL^{33}(py)_2]$	HS	–
	$[FeL^{44}(py)_2]$	HS	–
	$[FeL^{55}(py)_2]$	Abrupt	105
	$[FeL^{66}(py)_2]$	Abrupt	175
This work	$[FeL^{15}(py)_2]$	Gradual	315[a]
	$[FeL^{16}(py)_2]$	Gradual, stepwise	196[b]
	$[FeL^{25}(py)_2]$	HS	–
	$[FeL^{26}(py)_2]$	HS	–
	$[FeL^{34}(py)_2]$	HS	–
	$[FeL^{56}(py)_2]$	Gradual, incomplete	88[c]
	$[FeL^{14}(bpee)]_n$	HS	–
	$[FeL^{15}(bpee)]_n$	Gradual, incomplete	220[c]
	$[FeL^{16}(bpee)]_n$	Incomplete, with hysteresis	↓ 143; ↑ 150
	$[FeL^{25}(bpee)]_n$	HS	–
	$[FeL^{26}(bpee)]_n$	Gradual, incomplete	214[c]
	$[FeL^{34}(bpee)]_n$	HS	–
	$[FeL^{56}(bpee)]_n$	Gradual	227

[a]Estimated, assuming a $\chi_M T$ value of 3.5 cm^3 K mol^{-1} for the pure HS state. [b]First transition midpoint. [c]Inflection point.

$[FeL_{15}(py)_2]$ undergoes a gradual SCO with a very high transition temperature. The spin transition of $[FeL^{15}(py)_2]$ is very sluggish below 250 K but, more importantly, does not fully transition to the HS state even upon heating to 350 K. An estimated $T_{1/2}$ of 315 K is derived, assuming a $\chi_M T$ value of 3.5 cm^3 K mol^{-1} for the pure HS state. In comparison, its symmetric references $[FeL^{11}(py)_2]$ and $[FeL^{55}(py)_2]$ exhibit significantly lower $T_{1/2}$ values of 220 and 105 K, respectively.

$[FeL^{16}(py)_2]$ undergoes a complete, gradual two-step SCO. The first step begins above 160 K and reaches a slightly inclined plateau around 270 K, with $\gamma_{HS} = 0.61$. Upon further heating, the complete HS state is reached at 350 K. Upon cooling in the second cycle, about 24% of the iron centers remain in the HS state, suggesting the loss of ability to transition back into the LS state. The first transition midpoint lies at 196 K, intermediate between the $T_{1/2}$ values of $[FeL^{11}(py)_2]$ and $[FeL^{66}(py)_2]$. $[FeL^{56}(py)_2]$ shows an incomplete SCO, with an inflection point around 88 K and $\gamma_{HS} = 0.61$ at 50 K. The transition occurs at a lower temperature than those of its symmetrical counterparts.

2.13. Magnetic Properties of Coordination Polymers

The $\chi_M T$ versus T plots of the bpee coordination polymers are shown in Figure S24, Supporting Information. $[FeL^{25}(bpee)]_n$, and $[FeL^{34}(bpee)]_n$ remain in the HS state across the full temperature range, mirroring the behavior of their pyridine counterparts. $[FeL^{14}(bpee)]_n$ also remains in the HS state, consistent with the nature of the substituent $x = 4$, which is known to impede SCO. $[FeL^{15}(bpee)]_n$ undergoes a slow, gradual, and incomplete SCO between 350 and 50 K, with $\gamma_{HS} = 0.59$ at 50 K. $[FeL^{16}(bpee)]_n$ displays an incomplete spin transition with a narrow hysteresis with $T_{1/2}\downarrow = 143$ K, $T_{1/2}\uparrow = 150$ K, and a $\gamma_{HS} = 0.75$ at 50 K. This behavior

stands in contrast with the complete SCO seen in $[FeL^{16}(py)_2]$. $[FeL^{26}(bpee)]_n$, unlike its pyridine analo, shows an incomplete gradual SCO between 350 and 150 K with $\gamma_{HS} = 0.64$ at 150 K. $[FeL^{56}(bpee)]_n$ is the only coordination polymer exhibiting a complete spin transition, with $T_{1/2} = 227$ K. Interestingly, the transition is more complete and occurs at a significantly higher temperature than in the corresponding pyridine complex.

3. Conclusions

SCO remains among the most fascinating yet least predictable phenomena in coordination chemistry. While molecular design can tune the ligand field strength and influence the intrinsic energetics of the spin transition, the SCO behavior in the solid state is strongly governed by intermolecular cooperativity—a property that is notoriously difficult to anticipate from the molecular structure alone. Even subtle changes in molecular symmetry, crystal packing, or hydrogen bonding can profoundly alter the dynamics of the spin transition, ranging from abrupt transitions with hysteresis, to gradual, incomplete transitions.

In this work, we explored a mixed-substitution approach using seven novel, asymmetrically functionalized Jäger-ligands, with the goal of determining whether the asymmetric substitution leads to averaged properties compared to their symmetric references. Our results show that the outcome is more nuanced. While optical and electrochemical properties often reflect additive substitution effects, the SCO behavior of the iron(II) complexes deviates significantly. In some cases, asymmetric substitution suppresses SCO altogether despite both symmetric references exhibiting transitions, as in $[FeL^{25}(py)_2]$ and $[FeL^{26}(py)_2]$. In other systems, new SCO profiles arise, with distinct transition temperatures and slopes (e.g., $[FeL^{15}(py)_2]$, $[FeL^{16}(py)_2]$). This highlights that SCO in the bulk cannot be predicted solely from substitution patterns, but rather that the interplay between molecular symmetry and the resulting effects within the crystal packing must be considered.

The electrochemical data adds further weight to our earlier findings that electron-withdrawing substituents do not generally stabilize the HS state, contrary to earlier rules suggested in literature.[9] While strongly electron-withdrawing groups such as CF_3 clearly stabilize the iron(II) oxidation state, they do not impede SCO. Instead, the decisive factor appears to be the coordination mode of the chelating carbonyl: ketone carbonyl donors enable SCO, whereas ester-carbonyls stabilize the HS state and can suppress spin transitions altogether. This provides a more reliable structure–property correlation than substituent electronegativity alone.

The crystallographic analysis underscores the difficulty of predicting cooperativity. While the space group itself is not a reliable indicator, the dimensionality and continuity of intermolecular interactions are decisive. Reduced symmetry in the asymmetric complexes disrupts these networks and correlates with more gradual, less cooperative transitions compared to their symmetric analogs. Since reliable prediction of crystal packing is still elusive, design strategies that maximize symmetry and utilize functional groups or axial ligands capable of strong, directional interactions offer the greatest potential for increasing cooperativity.

Overall, our results emphasize that while electronic substitution effects are often additive and predictable at the molecular level, cooperativity in SCO remains a collective property of the crystal lattice, highly sensitive to symmetry and intermolecular interactions. Asymmetric substitution therefore offers a valuable tool not only for tuning intrinsic properties, but also for deliberately modulating cooperativity.

4. Experimental Section

Elemental analyses were conducted using a Unicube (Elementar Analysensysteme GmbH, Langenselbold, Germany) with sulfanilamide as standard. NMR spectra were recorded using a Avance III HD 500 MHz spectrometer (Bruker, Ettlingen, Germany) at 25 °C. UV–vis spectra were recorded using a Cary 60 UV–vis spectrometer (Agilent, Santa Clara, USA) with a scan rate of 600 nm min^{-1}.

SC-XRD: The single-crystal X-ray intensity data were collected on a Bruker-Nonius Kappa-CCD diffractometer equipped with a Mo-Kα IμS microfocus source and an Apex2 CCD detector. The crystal structures were solved with SHELXT-2018/3[67] and refined by full matrix least-squares methods on F^2 with ShelXT-2018/3,[68] using the Olex2 1.2 environment.[69] Multiscan absorption correction was applied to the intensity data.[70]

Magnetic Measurements: Magnetic measurements were carried out using a Quantum Design MPMS-XL-5 SQUID magnetometer (Quantum Design, San Diego, USA). The samples were prepared in a gelatin capsule, with a plastic straw as sample holder. A field strength of 0.5 T was applied, and the samples were measured in a temperature range of 5–350 K. The measured values were corrected for diamagnetism of the sample holder and the ligand (tabulated Pascal constants).[71]

CV: Redox potentials were determined by CV using an electrochemical analyzer CHI610E (CH Instruments, Inc. Austin, USA). The samples ($c = 1.0 \times 10^{-3}$ M) were measured at room temperature in pyridine with (n-Bu_4N)(PF_6) ($c = 0.1$ M) as electrolyte and a RHE reference at scan rates of 50, 100, 500, and 1000 mV s^{-1}. The potentials are given in reference to theferrocene/ferrocenium redox couple.

Computational Details: DFT calculations were performed using ORCA2.9.1.[72] large def2-TZVP basis sets[73] were used throughout. The structures of the ligands and iron(II) complexes were optimized with the generalized gradient approximation functional BP86;[74] complexes were optimized in both their LS and HS states. Cartesian coordinates of all optimized structures were compiled in the COORDINATES file (Tables c-xxx to c-yyy). To assess the SCO energies, five derivatives of the well-established hybrid functional B3LYP[56,75,76] were used in single-point calculations. In these derivative functionals, the amount of exact exchange a_0 was varied stepwise from 0.20 (native B3LYP) to 0.00. Dispersion contributions were approximated using Grimme's DFT-D3 atom pairwise dispersion corrections of the parent B3LYP functional.[77] Solvent effects were accounted for in a dielectric continuum approach (COSMO),[78] parametrized for MeCN. Molecular orbitals and electronic properties were extracted from single-point calculations in the optimized positions with the global hybrid functional TPSSh.[79] For each complex, the 70–90 lowest optical electronic transitions were assessed with ORCA implemented TD-DFT methods within the Tamm–Dancoff approximation.

Syntheses: $[Fe(OAc)_2]$ was synthesized as described in literature.[80] The preligands ${}_{pre}L^x$ ($x = 1, 2, 3, 5$) were obtained by stoichiometric reaction of o-phenylene diamine with the desired first keto-enol ether K^x as described by Jäger.[1,51] The asymmetrical ligands were obtained through reaction of the preligands ${}_{pre}L^x$ with the respective second keto-enol ether K^y in MeOH or EtOH. Due to E/Z-isomerism of

both enamine functions within the ligands, the number of NMR signals is up to quadrupled, often overlapping and with individual ratios depending on the substituents. Assignment of the signals can be found in the Supporting Information.

H_2L^{14}: $_{pre}L^1$ (427 mg, 1.72 mmol, 1 eq) and *KEE*[4] (291 mg, 1.72 mmol, 1 eq) were dissolved in EtOH (15 mL) and heated to 70 °C for 1 h. Solvent was removed, yielding a viscose, red oil. Pure product was obtained by recrystallization from EtOH/Et_2O mixture and subsequent recrystallization from EtOH, yielding white needles. Yield: 269 mg (42%). Elemental analysis for $C_{19}H_{21}N_3O_5$ (371.39 g mol^{-1}): found (calc.): C 61.40 (61.45), H 5.82 (5.70), N 11.24 (11.31). ^{1}H NMR (500 MHz, DMSO-d^6, 25 °C): $\delta = 12.80–12.37$ (m, 1H), 10.83–10.33 (m, 1H), 8.58–7.95 (m, 2H), 7.71–7.21 (m, 4H), 4.31–4.10 (m, 4H), 2.46–2.36 (m, 3H), 1.34–1.16 (m, 6H). ^{13}C NMR (126 MHz, DMSO, 25 °C): $\delta = 198.25$, 198.10, 166.24, 166.21, 165.95, 164.43, 157.57, 156.63, 154.58, 153.47, 134.16, 133.14, 132.50, 132.16, 128.39, 127.49, 127.10, 126.76, 125.47, 122.61, 121.56, 119.92, 118.09, 115.86, 102.92, 102.88, 75.10, 74.44, 60.51, 60.32, 59.52, 59.47, 39.52, 30.74, 30.73, 14.35, 14.31, 14.23. UV–vis (MeCN, 298 K): λ_{max} (ε) = 239 nm (1.0×10^6 L mol^{-1} cm^{-1}), 293 nm (3.2×10^6 L mol^{-1} cm^{-1}), 338 nm (2.4×10^6 L mol^{-1} cm^{-1}).

H_2L^{15}: $_{pre}L^1$ (372 mg, 1.50 mmol, 1 eq) and *KEE*[5] (313 mg, 1.53 mmol, 1.02 eq) were dissolved in EtOH (9 mL) and heated to 70 °C for 1 h. Solvent was removed, yielding a viscose, yellow oil. Pure product was obtained by recrystallization from Et_2O and subsequent recrystallization from EtOH, yielding yellow needles. Yield: 370 mg (59%). Elemental analysis for $C_{24}H_{24}N_2O_5$ (420.47 g mol^{-1}): found (calc.): C 68.40 (68.56), H 5.52 (5.75), N 6.40 (6.66). ^{1}H NMR (500 MHz, DMSO, 25 °C) δ 12.56–12.43 (m, 0.9H), 12.41–12.27 (m, 0.9H), 11.07 (s, 0.1H), 10.68–10.54 (m, 0.1H), 8.27–8.15 (m, 1.2H), 7.73–7.63 (m, 2.8H), 7.57–7.24 (m, 7H), 4.32–4.11 (m, 2H), 2.47–2.40 (m, 2.6H), 2.40–2.33 (m, 3H), 2.21 (s, 0.4H), 1.33–1.22 (m, 3H). ^{13}C NMR (126 MHz, DMSO-d^6) $\delta = 198.96$, 198.23, 194.20, 166.20, 156.12, 154.55, 139.82, 132.87, 132.83, 131.53, 129.07, 128.41, 127.29, 127.22, 121.70, 121.60, 112.41, 103.00, 59.49, 39.52, 30.74, 30.27, 27.30, 14.31, 14.21. UV–vis (MeCN, 298 K): λ_{max} (ε) = 240 nm (1.8×10^6 L mol^{-1} cm^{-1}), 299 nm (3.1×10^6 L mol^{-1} cm^{-1}), 344 nm (2.4×10^6 L mol^{-1} cm^{-1}).

H_2L^{16}: $_{pre}L^1$ (497 mg, 2.00 mmol, 1 eq) and *KEE*[6] (600 mg, 2.50 mmol, 1.25 eq) were dissolved in EtOH (12 mL) and heated to 70 °C for 30 min. Product crystallized from solution after storing at −20 °C and was purified by recrystallization from EtOH, yielding fine, white needles. Yield: 730 mg (82%). Elemental analysis for $C_{20}H_{21}F_3N_2O_6$ (442.39 g mol^{-1}): found (calc.): C 54.02 (54.30), H 4.84 (4.78), N 6.37 (6.33). ^{1}H NMR (500 MHz, DMSO, 25 °C): $\delta = 12.50–12.36$ (m, 1H), 12.00–11.91 (m, 1H), 11.16–11.05 (m, 1H), 10.66–10.57 (m, 1H), 8.33–8.12 (m, 2H), 7.60–7.32 (m, 4H), 4.30–4.11 (m, 4H), 2.44–2.34 (m, 3H), 1.32–1.17 (m, 6H). ^{13}C NMR (126 MHz, DMSO, 25 °C): $\delta = 198.08$, 194.04, 176.81, 166.23, 165.31, 164.41, 160.15, 158.08, 154.48, 154.42, 134.33, 134.08, 132.74, 132.65, 128.93, 128.51, 127.12, 124.23, 123.73, 121.33, 117.92, 115.63, 102.99, 102.93, 98.84, 98.59, 60.32, 60.27, 59.74, 59.48, 39.52, 30.76, 30.35, 14.30, 13.97, 13.83. UV–vis (MeCN, 298 K): λ_{max} (ε) = 240 nm (1.8×10^6 L mol^{-1} cm^{-1}), 307 nm (2.9×10^6 L mol^{-1} cm^{-1}), 348 nm (2.1×10^6 L mol^{-1} cm^{-1}).

H_2L^{25}: $_{pre}L^2$ (1.08 g, 4.95 mmol, 1 eq) and *KEE*[5] (1.01 g, 4.95 mmol, 1 eq) were dissolved in EtOH (40 mL) and heated to reflux for 1 h. Product crystallized immediately upon cooling and was purified by recrystallization from EtOH, yielding yellow needles. Yield: 1.37 g (71%). Elemental analysis for $C_{23}H_{22}N_2O_4$ (390.44 g mol^{-1}): found (calc.): C 70.62 (70.75), H 5.55 (5.68), N 7.08 (7.18). ^{1}H NMR (500 MHz, DMSO, 25 °C) $\delta = 12.53$ (d, $J = 12.5$ Hz, 1H), 12.39 (d, $J = 12.7$ Hz, 0.9H), 11.14 (s, 0.1H), 8.32–8.24 (m, 1H), 8.20 (d, $J = 12.9$ Hz, 0.1H), 7.73–7.59 (m, 3.7H), 7.58–7.24 (m, 6.2H), 2.42 (s, 2.6H), 2.39–2.32 (m, 6H), 2.21 (s, 0.4H). ^{13}C NMR (126 MHz, DMSO, 25 °C): $\delta = 199.38$, 199.07, 195.30, 194.18, 156.12, 155.56, 139.81, 132.82, 132.56, 131.54, 129.06, 128.42, 128.00, 127.86, 127.17, 126.99, 121.71, 121.62, 113.38, 112.43, 39.52, 31.59, 30.26, 27.46. UV–vis (MeCN, 298 K): λ_{max} (ε) = 249 nm (1.4×10^6 L mol^{-1} cm^{-1}), 300 nm (3.3×10^6 L mol^{-1} cm^{-1}), 348 nm (2.5×10^6 L mol^{-1} cm^{-1}).

H_2L^{26}: $_{pre}L^2$ (873 mg, 4.00 mmol, 1 eq) was stirred in EtOH (30 mL), before *KEE*[6] (970 mg, 4.04 mmol, 1.01 eq) was added. The mixture was heated to 70 °C and stirred until everything was solved, then stirred for an additional 10 min. Solvent was removed, yielding a viscose, orange oil. Pure product was obtained after crystallizing twice from a mixture of EtOH and Et_2O, yielding a yellow solid. Yield: 592 mg (36%). Elemental analysis for $C_{19}H_{19}F_3N_2O_5$ (412.37 g mol^{-1}): found (calc.): C 55.58 (55.34), H 4.77 (4.64), N 6.62 (6.79). ^{1}H NMR (500 MHz, DMSO, 25 °C) $\delta = 12.52–12.39$ (m, 1H), 12.04–11.92 (m, 0.6H), 11.17–11.07 (m, 0.3H), 8.33–8.19 (m, 1.6H), 8.19–8.11 (m, 0.4H), 7.75–7.65 (m, 1H), 7.63–7.50 (m, 1H), 7.50–7.40 (m, 1H), 7.40–7.32 (m, 1H), 4.27 (q, $J = 7.1$ Hz, 0.7H), 4.17 (q, $J = 7.1$ Hz, 1.3H), 2.42–2.29 (m, 6H), 1.29–1.20 (m, 3H). ^{13}C NMR (126 MHz, DMSO, 25 °C): $\delta = 199.22$, 195.30, 177.13, 176.85, 165.36, 164.39, 160.13, 158.05, 155.35, 155.24, 134.30, 134.06, 132.41, 128.81, 128.40, 126.86, 124.17, 123.65, 121.34, 113.42, 113.37, 98.87, 98.62, 60.36, 60.29, 39.52, 31.59, 27.44, 13.97, 13.83. UV–vis (MeCN, 298 K): λ_{max} (ε) = 251 nm (2.1×10^6 L mol^{-1} cm^{-1}), 306 nm (3.0×10^6 L mol^{-1} cm^{-1}), 344 nm (2.2×10^6 L mol^{-1} cm^{-1}).

H_2L^{34}: $_{pre}L^3$ (835 mg, 3.00 mmol, 1 eq) and *KEE*[4] (508 mg, 3.00 mmol, 1 eq) were dissolved in EtOH (20 mL) and heated to reflux for 1 h. The product crystallized upon cooling as yellow crystals. Yield: 900 mg (74%). Elemental analysis for $C_{20}H_{23}N_3O_6$ (401.42 g mol^{-1}): found (calc.): C 59.86 (59.84), H 5.73 (5.78), N 10.36 (10.47). ^{1}H NMR (500 MHz, DMSO, 25 °C) $\delta = 10.89–10.18$ (m, 2H), 8.51–7.96 (m, 2H), 7.61–7.12 (m, 4H), 4.26–4.06 (m, 6H), 1.29–1.18 (m, 9H). ^{13}C NMR (126 MHz, DMSO, 25 °C): $\delta = 167.19$, 166.86, 166.08, 164.86, 164.43, 157.52, 156.31, 154.34, 153.30, 134.33, 133.20, 132.63, 132.12, 128.28, 127.26, 126.81, 126.27, 125.15, 122.00, 121.82, 120.03, 118.10, 115.91, 93.99, 75.03, 74.28, 60.49, 60.32, 59.74, 59.63, 59.50, 59.44, 39.52, 18.59, 14.35, 14.29, 14.24, 14.22. UV–vis (MeCN, 298 K): λ_{max} (ε) = 287 nm (2.6×10^6 L mol^{-1} cm^{-1}), 328 nm (2.0×10^6 L mol^{-1} cm^{-1}).

H_2L^{56}: $_{pre}L^5$ (960 mg, 3.43 mmol, 1 eq) was dissolved in EtOH (25 mL) through heating, before *KEE*[6] (910 mg, 3.79 mmol, 1.1 eq) was added and the solution was heated to 70 °C for 20 min. The product crystallized upon cooling and was purified by recrystallized from EtOH, yielding yellow crystals. Yield: 870 mg (48%). Elemental analysis for $C_{24}H_{21}F_3N_2O_5$ (474.44 g mol^{-1}): found (calc.): C 60.42 (60.76), H 4.43 (4.46), N 5.99 (5.90). ^{1}H NMR (500 MHz, DMSO, 25 °C) $\delta = 12.38–12.25$ (m, 0.8H), 12.03–11.93 (m, 0.5H), 11.18–11.00 (m, 0.4H), 8.32–8.25 (m, 0.6H), 8.18–8.12 (m, 0.5H), 7.72–7.63 (m, 2.7H), 7.63–7.26 (m, 7H), 4.38–4.13 (m, 2H), 2.42–2.34 (m, 2.6H), 2.24–2.20 (m, 0.4H), 1.31–1.21 (m, 3H). ^{13}C NMR (126 MHz, DMSO, 25 °C): $\delta = 198.87$, 194.25, 182.26, 164.42, 160.12, 155.92, 139.81, 134.47, 132.81, 131.55, 129.07, 128.83, 128.43, 127.86, 127.07, 124.13, 121.31, 112.49, 98.87, 60.29, 39.52, 30.31, 13.99, 13.85. UV–vis (MeCN, 298 K): λ_{max} (ε) = 245 nm (1.9×10^6 L mol^{-1} cm^{-1}), 306 nm (2.9×10^6 L mol^{-1} cm^{-1}), 345 nm (2.6×10^6 L mol^{-1} cm^{-1}).

[FeL^{14}(EtOH)$_2$]: H_2L^{14} (186 mg, 0.50 mmol, 1 eq) and [Fe(OAc)$_2$] (131 mg, 0.75 mmol, 1.5 eq) were dissolved in EtOH (10 mL) and heated to reflux for 1 h. After cooling, the solution was narrowed to half its volume and stored at −20 °C. The precipitate was filtered off, washed with EtOH (2 × 1 mL) and dried under reduced pressure, yielding the product as black crystals. Yield: 140 mg (54%). Elemental analysis for $C_{23}H_{31}FeN_3O_7$ (517.36 g mol^{-1}): found (calc.): C 53.40 (53.40), H 5.55 (6.04), N 8.09 (8.12).

[FeL^{14}(py)$_2$] (in situ): UV–vis (pyridine, 298 K): λ_{max} (ε) = 324 nm (3.9×10^6 L mol^{-1} cm^{-1}), 367 nm (2.5×10^6 L mol^{-1} cm^{-1}), 527 nm (1.6×10^7 L mol^{-1} cm^{-1}).

[FeL^{15}(py)$_2$]: H_2L^{15} (252 mg, 0.60 mmol, 1 eq) and [Fe(OAc)$_2$] (157 mg, 0.90 mmol, 1.5 eq) were dissolved in a mixture of EtOH (6 mL) and

pyridine (2 mL). The solution was heated to reflux for 1 h. After cooling, H_2O (6 mL) was added to the solution and stored at 6 °C. The precipitate was filtered off, washed with EtOH (2 × 3 mL) and dried under reduced pressure, yielding the product as black crystals. Yield: 42 mg (11%). Elemental analysis for $C_{34}H_{32}FeN_4O_5$ (632.50 g mol^{-1}): found (calc.): C 64.15 (64.57), H 4.79 (5.10), N 8.69 (8.86). UV–vis (pyridine, 298 K): λ_{max} (ε) = 329 nm (3.6 × 10^6 L mol^{-1} cm^{-1}), 367 nm (2.2 × 10^6 L mol^{-1} cm^{-1}), 541 nm (1.5 × 10^7 L mol^{-1} cm^{-1}).

[FeL^{16}(py)$_2$]: H_2L^{16} (76 mg, 0.17 mmol, 1 eq) and [Fe(OAc)$_2$] (45 mg, 0.26 mmol, 1.5 eq) were dissolved in a mixture of EtOH (1.2 mL) and pyridine (0.6 mL). The solution was heated to reflux for 1 h. After cooling, H_2O (1 mL) was added to the solution and stored at 6 °C. The precipitate was filtered off, washed with EtOH (2 × 0.4 mL) and dried under reduced pressure, yielding the product as black crystals. Yield: 38 mg (34%). Elemental analysis for $C_{30}H_{29}F_3FeN_4O_6$ (654.42 g mol^{-1}): found (calc.): C 54.94 (55.06), H 4.33 (4.47), N 8.44 (8.56). UV–vis (pyridine, 298 K): λ_{max} (ε) = 335 nm (2.8 × 10^6 L mol^{-1} cm^{-1}), 567 nm (1.0 × 10^7 L mol^{-1} cm^{-1}).

[FeL^{25}(py)$_2$]: H_2L^{25} (390 mg, 1.00 mmol, 1 eq) and [Fe(OAc)$_2$] (261 mg, 1.50 mmol, 1.5 eq) were dissolved in a mixture of EtOH (6 mL) and pyridine (1.5 mL). The solution was heated to reflux for 1 h. After cooling, the solution was narrowed to half its volume and stored at −20 °C. The precipitate was filtered off, washed with EtOH (2 × 1 mL) and dried under reduced pressure, yielding the product as brown needles. Yield: 142 mg (23%). Elemental analysis for $C_{33}H_{30}FeN_4O_4$ (602.47 g mol^{-1}): found (calc.): C 65.39 (65.79), H 4.72 (5.02), N 9.22 (9.30). UV–vis (pyridine, 298 K): λ_{max} (ε) = 331 nm (4.1 × 10^6 L mol^{-1} cm^{-1}), 367 nm (2.5 × 10^6 L mol^{-1} cm^{-1}), 543 nm (1.8 × 10^7 L mol^{-1} cm^{-1}).

[FeL^{26}(py)$_2$]: H_2L^{26} (165 mg, 0.40 mmol, 1 eq) and [Fe(OAc)$_2$] (104 mg, 0.60 mmol, 1.5 eq) were dissolved in a mixture of MeOH (2 mL) and pyridine (0.7 mL). The solution was heated to reflux for 1 h. The solution was stored at −20 °C. Heating the solution to room temperature led to spontaneous crystallisation of the product. The precipitate was filtered off, washed with MeOH (2 × 1.4 mL) and dried under reduced pressure, yielding the product as brown powder. Yield: 158 mg (63%). Elemental analysis for $C_{29}H_{27}F_3FeN_4O_5$ (624.40 g mol^{-1}): found (calc.): C 55.47 (55.78), H 4.14 (4.36), N 8.96 (8.97). UV–vis (pyridine, 298 K): λ_{max} (ε) = 336 nm (3.1 × 10^6 L mol^{-1} cm^{-1}), 568 nm (1.1 × 10^7 L mol^{-1} cm^{-1}).

[FeL^{34}(py)$_2$]: H_2L^{34} (321 mg, 0.80 mmol, 1 eq) and [Fe(OAc)$_2$] (209 mg, 1.20 mmol, 1.5 eq) were dissolved in a mixture of EtOH (10 mL) and pyridine (5 mL). The solution was heated to reflux for 1 h. After storing at −20 °C, the precipitate was filtered off, washed with EtOH (2 × 1.2 mL) and dried under reduced pressure, yielding the product as red-brown crystals. Yield: 158 mg (32%). Elemental analysis for $C_{30}H_{31}FeN_5O_6$ (613.45 g mol^{-1}): found (calc.): C 58.69 (58.74), H 4.98 (5.09), N 11.54 (11.42). UV–vis (pyridine, 298 K): λ_{max} (ε) = 317 nm (3.4 × 10^6 L mol^{-1} cm^{-1}), 365 nm (2.4 × 10^6 L mol^{-1} cm^{-1}), 493 nm (1.3 × 10^7 L mol^{-1} cm^{-1}).

[FeL^{56}(py)$_2$]: H_2L^{56} (190 mg, 0.40 mmol, 1 eq) and [Fe(OAc)$_2$] (104 mg, 0.60 mmol, 1.5 eq) were dissolved in a mixture of MeOH (2 mL) and pyridine (0.7 mL). The solution was heated to reflux for 1 h. The solution was stored at −20 °C. Heating the solution to room temperature led to spontaneous crystallisation of the product. The precipitate was filtered off, washed with MeOH (2 × 1 mL) and dried under reduced pressure, yielding the product as black crystals. Yield: 212 mg (77%). Elemental analysis for $C_{34}H_{29}F_3FeN_4O_5$ (686.47 g mol^{-1}): found (calc.): C 59.26 (59.49), H 4.22 (4.26), N 8.22 (8.16). UV–vis (pyridine, 298 K): λ_{max} (ε) = 337 nm (3.1 × 10^6 L mol^{-1} cm^{-1}), 565 nm (1.2 × 10^7 L mol^{-1} cm^{-1}).

Coordination polymers were all synthesized by dissolving ≈60 mg of the respective EtOH or pyridine complex in 10 mL of EtOH or MeOH, addition of 8 eq. of 1,2-di(4-pyridyl) ethylene and heating under reflux for 3 h. After cooling, the precipitate was filtered off, washed with EtOH (H_2L^{14}, H_2L^{15}, H_2L^{16}, H_2L^{25}, H_2L^{34}) or MeOH (H_2L^{26}, H_2L^{56}) (2 × 2.5 mL) and dried under reduced pressure, yielding the desired product.

[FeL^{14}(bpee)]$_n$. Elemental analysis for $C_{31}H_{29}FeN_5O_5$ (607.45 g mol^{-1}): found (calc.): C 61.15 (61.30), H 4.69 (4.81), N 11.43 (11.53).

[FeL^{15}(bpee)]$_n$. Elemental analysis for $C_{36}H_{32}FeN_4O_5$ (656.52 g mol^{-1}): found (calc.): C 65.38 (65.86), H 4.87 (4.91), N 8.34 (8.53).

[FeL^{16}(bpee)]$_n$. Elemental analysis for $C_{32}H_{29}F_3FeN_4O_6$ (678.45 g mol^{-1}): found (calc.): C 56.43 (56.65), H 4.43 (4.31), N 8.14 (8.26).

[FeL^{25}(bpee)]$_n$. Elemental analysis for $C_{35}H_{30}FeN_4O_4$ (626.49 g mol^{-1}): found (calc.): C 66.81 (67.10), H 4,51 (4.83), N 8.61 (8.94).

[FeL^{26}(bpee)]$_n$. Elemental analysis for $C_{31}H_{27}F_3FeN_4O_5$ (648.42 g mol^{-1}): found (calc.): C 57.66 (57.42), H 4.29 (4.20), N 8.81 (8.64).

[FeL^{34}(bpee)]$_n$. Elemental analysis for $C_{32}H_{31}FeN_5O_6$ (637.47 g mol^{-1}): found (calc.): C 59.95 (60.29), H 4,79 (4.90), N 10.96 (10.99).

[FeL^{56}(bpee)]$_n$. Elemental analysis for $C_{36}H_{29}F_3FeN_4O_5$ (710.49 g mol^{-1}): found (calc.): C 60.39 (60.86), H 3.91 (4.11), N 7.91 (7.89).

Acknowledgements

Financial support from the German Research Foundation (DFG; project numbers 463161096, 509879467) is gratefully acknowledged.

Open Access funding enabled and organized by Projekt DEAL.

Conflict of Interest

The authors declare no conflict of interest.

Data Availability Statement

The data that support the findings of this study are available from the corresponding author upon reasonable request.

Keywords: asymmetric ligands · density functional theory · mixed substitution · Schiff base · spin-crossover

[1] L. Fabbrizzi, A. Poggi, *Chemistry at the Beginning of the Third Millennium*, Springer, Berlin, Heidelberg **2000**.
[2] M. Rudolph, S. Dautz, E.-G. Jäger, *J. Am. Chem. Soc.* **2000**, *122*, 10821.
[3] H. Kurz, C. Hils, J. Timm, G. Hörner, A. Greiner, R. Marschall, H. Schmalz, B. Weber, *Angew. Chem., Int. Ed.* **2022**, *61*, e202117570.
[4] H. Kurz, G. Hörner, O. Weser, G. L. Manni, B. Weber, *Chem. Eur. J.* **2021**, *27*, 15158.
[5] H. Kurz, K. Schötz, I. Papadopoulos, F. W. Heinemann, H. Maid, D. M. Guldi, A. Köhler, G. Hörner, B. Weber, *J. Am. Chem. Soc.* **2021**, *143*, 3466.
[6] H. Kurz, G. Hörner, B. Weber, *Z. Anorg. Allg. Chem.* **2021**, *647*, 896.
[7] H. Kurz, J. Sander, B. Weber, *Z. Anorg. Allg. Chem.* **2020**, *646*, 800.
[8] H.-Y. Sun, K.-Y. Wang, L. Zhao, R.-H. Zhou, Y.-S. Meng, T. Liu, *Cryst. Growth Des.* **2025**, *25*, 3058.
[9] B. Weber, E.-G. Jäger, *Eur. J. Inorg. Chem.* **2009**, *2009*, 465.
[10] F. Daumann, G. Hörner, P. Köhler, B. Weber, *Cryst. Growth Des.* **2025**, *25*, 4565.
[11] M. A. Halcrow, *Spin-Crossover Materials. Properties and Applications*, Wiley, Chichester **2013**.
[12] P. Gütlich, *Eur. J. Inorg. Chem.* **2013**, *2013*, 581.

[13] G. Molnár, S. Rat, L. Salmon, W. Nicolazzi, A. Bousseksou, *Adv. Mater.* **2018**, *30*, 1703862.
[14] H. L. Feltham, A. S. Barltrop, S. Brooker, *Coord. Chem. Rev.* **2017**, *344*, 26.
[15] K. S. Kumar, Y. Bayeh, T. Gebretsadik, F. Elemo, M. Gebrezgiabher, M. Thomas, M. Ruben, *Dalton Trans.* **2019**, *48*, 15321.
[16] M. A. Halcrow, *Dalton Trans.* **2020**, *49*, 15560.
[17] A. Enriquez-Cabrera, A. Rapakousiou, M. P. Bello, G. Molnár, L. Salmon, A. Bousseksou, *Coord. Chem. Rev.* **2020**, *419*, 213396.
[18] E. Coronado, *Nat. Rev. Mater.* **2020**, *5*, 87.
[19] P. Guionneau, M. Marchivie, G. Chastanet, *Chem. Eur. J.* **2021**, *27*, 1483.
[20] M. Klaß, J. Krahmer, C. Näther, F. Tuczek, *Dalton Trans.* **2018**, *47*, 1261.
[21] H. Brandenburg, J. Krahmer, K. Fischer, B. Schwager, B. Flöser, C. Näther, F. Tuczek, *Eur. J. Inorg. Chem.* **2018**, *2018*, 576.
[22] K. Keisers, H. M. Hüppe, L. Iffland-Mühlhaus, A. Hoffmann, C. Göbel, U.-P. Apfel, B. Weber, S. Herres-Pawlis, *Inorg. Chem.* **2020**, *59*, 15343.
[23] M. Y. Da Xie, Z.-L. Xie, R. T. Kadakia, C. Chung, L. E. Ohman, K. Javanmardi, E. L. Que, *Angew. Chem., Int. Ed.* **2020**, *59*, 22523.
[24] C. T. Kelly, S. Dunne, I. A. Kühne, A. Barker, K. Esien, S. Felton, H. Müller-Bunz, Y. Ortin, G. G. Morgan, *Angew. Chem., Int. Ed.* **2023**, *62*, e202217388.
[25] C. Schreck, J. Weihermüller, P. Thoma, S. Rosenfeldt, M. Drechsler, C. Förster, K. Heinze, G. Hörner, B. Weber, *Eur. J. Inorg. Chem.* **2022**, e202200341.
[26] J. Weihermüller, S. Schlamp, B. Dittrich, B. Weber, *Inorg. Chem.* **2019**, *58*, 1278.
[27] S. Schönfeld, K. Dankhoff, D. Baabe, M.-K. Zaretzke, M. Bröring, K. Schötz, A. Köhler, G. Hörner, B. Weber, *Inorg. Chem.* **2020**, *59*, 8320.
[28] C. Schreck, S. Schönfeld, P. Liebing, G. Hörner, B. Weber, *Dalton Trans.* **2024**, *53*, 9092.
[29] S. Shaw, J. D. White, *Chem. Rev.* **2019**, *119*, 9381.
[30] C. J. Whiteoak, G. Salassa, A. W. Kleij, *Chem. Soc. Rev.* **2012**, *41*, 622.
[31] J. C. Pessoa, I. Correia, *Coord. Chem. Rev.* **2019**, *388*, 227.
[32] P. A. Vigato, S. Tamburini, *Coord. Chem. Rev.* **2004**, *248*, 1717.
[33] W. Zhou, W.-Q. Deng, X. Lu, *Interdiscip. Mater.* **2024**, *3*, 87.
[34] F. Bia, I. Gualandi, J. Griebel, L. Rasmussen, B. Hallak, D. Tonelli, B. Kersting, *J. Mater. Chem. C* **2023**, *11*, 2957.
[35] A. Erxleben, *Inorg. Chim. Acta* **2018**, *472*, 40.
[36] H. Görls, E.-G. Jäger, *Cryst. Res. Technol.* **1991**, *26*, 349.
[37] E.-G. Jäger, M. Rudolph, R. Müller, *Z. Chem.* **1978**, *18*, 229.
[38] S. Schönfeld, W. Bauer, S. Thallmair, G. Hörner, B. Weber, *Z. Anorg. Allg. Chem.* **2021**, *647*, 905.
[39] P. Middya, A. Saha, S. Chattopadhyay, *Inorg. Chim. Acta* **2023**, *545*, 121246.
[40] D. A. Annis, E. N. Jacobsen, *J. Am. Chem. Soc.* **1999**, *121*, 4147.
[41] E. Campbell, S. T. Nguyen, *Tetrahedron Lett.* **2001**, *42*, 1221.
[42] S. Curreli, E. C. Escudero-Adán, J. Benet-Buchholz, A. W. Kleij, *J. Org. Chem.* **2007**, *72*, 7018.
[43] S. Curreli, E. C. Escudero-Adán, J. Benet-Buchholz, A. W. Kleij, *Eur. J. Inorg. Chem.* **2008**, *2008*, 2863.
[44] M. Holbach, X. Zheng, C. Burd, C. W. Jones, M. Weck, *J. Org. Chem.* **2006**, *71*, 2903.
[45] A. W. Kleij, D. M. Tooke, A. L. Spek, J. N. H. Reek, *Eur. J. Inorg. Chem.* **2005**, *2005*, 4626.
[46] R. G. Konsler, J. Karl, E. N. Jacobsen, *J. Am. Chem. Soc.* **1998**, *120*, 10780.
[47] J. Lopez, S. Liang, X. R. Bu, *Tetrahedron Lett.* **1998**, *39*, 4199.
[48] L. Rigamonti, F. Demartin, A. Forni, S. Righetto, A. Pasini, *Inorg. Chem.* **2006**, *45*, 10976.
[49] D. Villaman, A. Vega, L. La Santa Maria de Parra, I. E. León, P. Levín, P. M. Toro, *Dalton Trans.* **2023**, *52*, 10855.
[50] W. Bauer, T. Ossiander, B. Weber, *Front. Chem. Sci. Eng.* **2018**, *12*, 400.
[51] E.-G. Jäger, *Z. Anorg. Allg. Chem.* **1967**, *349*, 139.
[52] W. Bauer, T. Ossiander, B. Weber, *Z. Naturforsch. B* **2010**, *65*, 323.
[53] H. Kurz, C. Lochenie, K. G. Wagner, S. Schneider, M. Karg, B. Weber, *Chem. Eur. J.* **2018**, *24*, 5100.
[54] B. Weber, *Coord. Chem. Rev.* **2009**, *253*, 2432.
[55] D. N. Bowman, E. Jakubikova, *Inorg. Chem.* **2012**, *51*, 6011.
[56] M. Reiher, O. Salomon, B. A. Hess, *Theor. Chem. Acc.* **2001**, *107*, 48.
[57] H. Petzold, P. Djomgoue, G. Hörner, C. Lochenie, B. Weber, T. Rüffer, *Dalton Trans.* **2018**, *47*, 491.
[58] H. Petzold, G. Hörner, L. Schnaubelt, T. Rüffer, *Dalton Trans.* **2018**, *47*, 17257.
[59] P. Stock, D. Wiedemann, H. Petzold, G. Hörner, *Inorganics (Basel)* **2017**, *5*, 60.
[60] E.-G. Jäger, J. Knaudt, M. Rudolph, M. Rost, *Chem. Ber.* **1996**, *129*, 1041.
[61] S. Schönfeld, G. Hörner, F. W. Heinemann, A. Hofmann, R. Marschall, B. Weber, *Z. Anorg. Allg. Chem.* **2021**, *647*, 295.
[62] A. Berkefeld, M. Fröhlich, M. Kordan, G. Hörner, H. Schubert, *Chem. Commun.* **2020**, *56*, 3987.
[63] L. Kletsch, G. Hörner, A. Klein, *Organometallics* **2020**, *39*, 2820.
[64] F. Maschietto, M. Campetella, J. S. García, C. Adamo, I. Ciofini, *J. Chem. Phys.* **2021**, *154*, 204102.
[65] E. G. Jäger, G. Leibeling, H. Görls, *CCDC 2264086: Experimental Crystal Structure Determination*, Cambridge Crystallographic Data Centre, Cambridge, UK **2023**.
[66] B. Weber, E. Kaps, J. Weigand, C. Carbonera, J.-F. Létard, K. Achterhold, F. G. Parak, *Inorg. Chem.* **2008**, *47*, 487.
[67] G. M. Sheldrick, *Acta Cryst. A* **2015**, *71*, 3.
[68] G. M. Sheldrick, *Acta Cryst. C* **2015**, *71*, 3.
[69] O. V. Dolomanov, L. J. Bourhis, R. J. Gildea, J. A. K. Howard, H. Puschmann, *J. Appl. Crystallogr.* **2009**, *42*, 339.
[70] Bruker AXS Inc, *Apex4 and SADABS*, Bruker AXS Inc, Madison, Wisconsin, USA **2001**.
[71] P. Day, *Science* **1994**, *266*, 145.
[72] F. Neese, *WIREs Comput. Mol. Sci.* **2012**, *2*, 73.
[73] A. Schäfer, H. Horn, R. Ahlrichs, *J. Chem. Phys.* **1992**, *97*, 2571.
[74] A. D. Becke, *Phys. Rev. A* **1988**, *38*, 3098.
[75] R. M. Dickson, A. D. Becke, *J. Chem. Phys.* **1993**, *99*, 3898.
[76] B. Miehlich, A. Savin, H. Stoll, H. Preuss, *Chem. Phys. Lett.* **1989**, *157*, 200.
[77] S. Grimme, J. Antony, S. Ehrlich, H. Krieg, *J. Chem. Phys.* **2010**, *132*, 154104.
[78] A. Klamt, G. Schüürmann, *J. Chem. Soc., Perkin Trans. 2* **1993**, 799.
[79] V. N. Staroverov, G. E. Scuseria, J. Tao, J. P. Perdew, *J. Chem. Phys.* **2003**, *119*, 12129.
[80] B. Weber, R. Betz, W. Bauer, S. Schlamp, *Z. Anorg. Allg. Chem.* **2011**, *637*, 102.

Manuscript received: September 3, 2025
Revised manuscript received: October 7, 2025
Version of record online: October 22, 2025